An update on the geology of northern Hogem batholith and its surroundings, north-central British Columbia

Luke Ootes[1, a], Anika L. Bergen[1], Dejan Milidragovic[1], Gabrielle O. Jones[1, 2], Alfredo Camacho[3], and Richard Friedman[4]

[1] British Columbia Geological Survey, Ministry of Energy, Mines and Petroleum Resources, Victoria, BC, V8W 9N3
[2] Department of Earth & Atmospheric Sciences, University of Alberta, Edmonton, AB, T6G 2E3
[3] Department of Geological Sciences, University of Manitoba, Winnipeg, MB, R3T 2N2
[4] Pacific Centre for Geochemical and Isotopic Research, University of British Columbia, Vancouver, BC, V6T 1Z4
[a] corresponding author: Luke.Ootes@gov.bc.ca

Recommended citation: Ootes, L., Bergen, A.L., Milidragovic, D., Jones, G.O., Camacho, A., and Friedman, R., 2020. An update on the geology of northern Hogem batholith and its surroundings, north-central British Columbia. In: Geological Fieldwork 2019, British Columbia Ministry of Energy, Mines and Petroleum Resources, British Columbia Geological Survey Paper 2020-01, pp. 25-47.

Abstract

New bedrock mapping refines the distribution and relationships of plutonic rocks in northern Hogem batholith and surrounding rocks in the Quesnel, Stikine, and Cache Creek terranes. Cutting the Quesnel terrane, the Hogem batholith is composed of ca. 197 Ma hornblendite and diorite of the Thane Creek suite, 182 to 178 Ma biotite pyroxenite and syenite of the Duckling Creek suite, ca. 160 Ma granite of the Osilinka suite, and ca. 174 Ma tonalite and 140 to 135 Ma granodiorite and granite of the Mesilinka suite. All units contain a penetrative foliation and $^{40}Ar/^{39}Ar$ biotite ages indicate post-deformation cooling and uplift after ca. 124 Ma. The Hogem batholith is bounded to the north and east by volcanic and sedimentary rocks of the Nicola Group (Triassic) along fault and intrusive contacts. To the west, Hogem batholith and Nicola Group are separated from the Cache Creek and Stikine terranes along the Pinchi-Ingenika dextral strike-slip fault system; farther west, an unexposed thrust fault juxtaposes Cache Creek rocks above Stikine terrane rocks. The Stikine terrane in the study area includes the Asitka Group (Carboniferous to Permian) volcano-sedimentary basement that is overlain by immature siliciclastic sedimentary rocks of the Dewar Formation (Takla Group; Triassic), and which is overlain by the Telkwa Formation (Hazelton Group; Jurassic). Cache Creek terrane encompasses metamorphic rocks of the Sitlika assemblage (Lower Jurassic), which have sedimentary and volcanic protoliths, serpentinites of the Trembleur ultramafic complex (Permian to Upper Triassic), mixed volcanic and metasedimentary rocks of the Sowchea succession (Upper Pennsylvanian to Lower Jurassic), and Cretaceous intrusive rocks of the Axelgold layered mafic intrusion. About 88 mineral occurrences in the area are documented in MINFILE. Seven new occurrences discovered in 2019; five of these close to previously recognized mineralization. When combined with results of 2018 mapping, 24 new mineral occurrences have been documented in the study area. Porphyry Cu ±Mo, Au in Hogem batholith is the predominant type followed by quartz-carbonate vein-hosted base and precious metals in Quesnel and Stikine terranes, and volcanic/sediment-hosted Cu in the Telkwa Formation of the Stikine terrane.

Keywords: Hogem batholith, Quesnel terrane, Stikine terrane, Cache Creek terrane, Cretaceous deformation, copper and gold, porphyry, veins, sediment-hosted

1. Introduction

In 2018, the British Columbia Geological Survey initiated a three-year mapping project in the Omineca Mountains of north-central British Columbia (Figs. 1, 2; Ootes et al., 2019a, b, 2020a). The project aims to better understand the bedrock and surficial geology and associated base- and precious-metal mineralization in the northern part of Hogem batholith. Detailed 1:50,000-scale mapping in 2019 included parts of NTS 93M/16, 93N/13, 94C/03, 04, 05, and 94D/01, 08 (Fig. 3; Ootes et al., 2020a). Herein we present the results of this mapping, which focussed on northern Hogem batholith and surrounding supracrustal, intrusive, and ultramafic rocks of the Quesnel, Stikine, and Cache Creek terranes; a companion full-scale map is presented elsewhere (Ootes et al., 2020a). We also present the preliminary results of new U-Pb zircon and $^{40}Ar/^{39}Ar$ biotite, hornblende, and muscovite geochronology and geochemical data, the details of which will also be presented elsewhere (Ootes et al., 2020b).

2. Geologic setting

The 2019 study area includes igneous intrusive rocks of northern Hogem batholith, metamorphosed volcanic and sedimentary rocks and less common intrusive rocks of the Quesnel and Stikine terranes, and metamorphic and ultramafic rocks of the Cache Creek terrane (Fig. 2). The Hogem batholith is bounded to the north and east by volcanic and sedimentary rocks of the Nicola Group (Triassic; Quesnel terrane) along fault and intrusive contacts (Figs. 2, 3). To the west, Hogem batholith and Nicola Group are juxtaposed against Cache Creek and Stikine terranes across the Pinchi-Ingenika dextral strike-slip fault system. The Stikine and Cache Creek terranes are separated by an unexposed thrust fault (Figs. 2, 3). To the

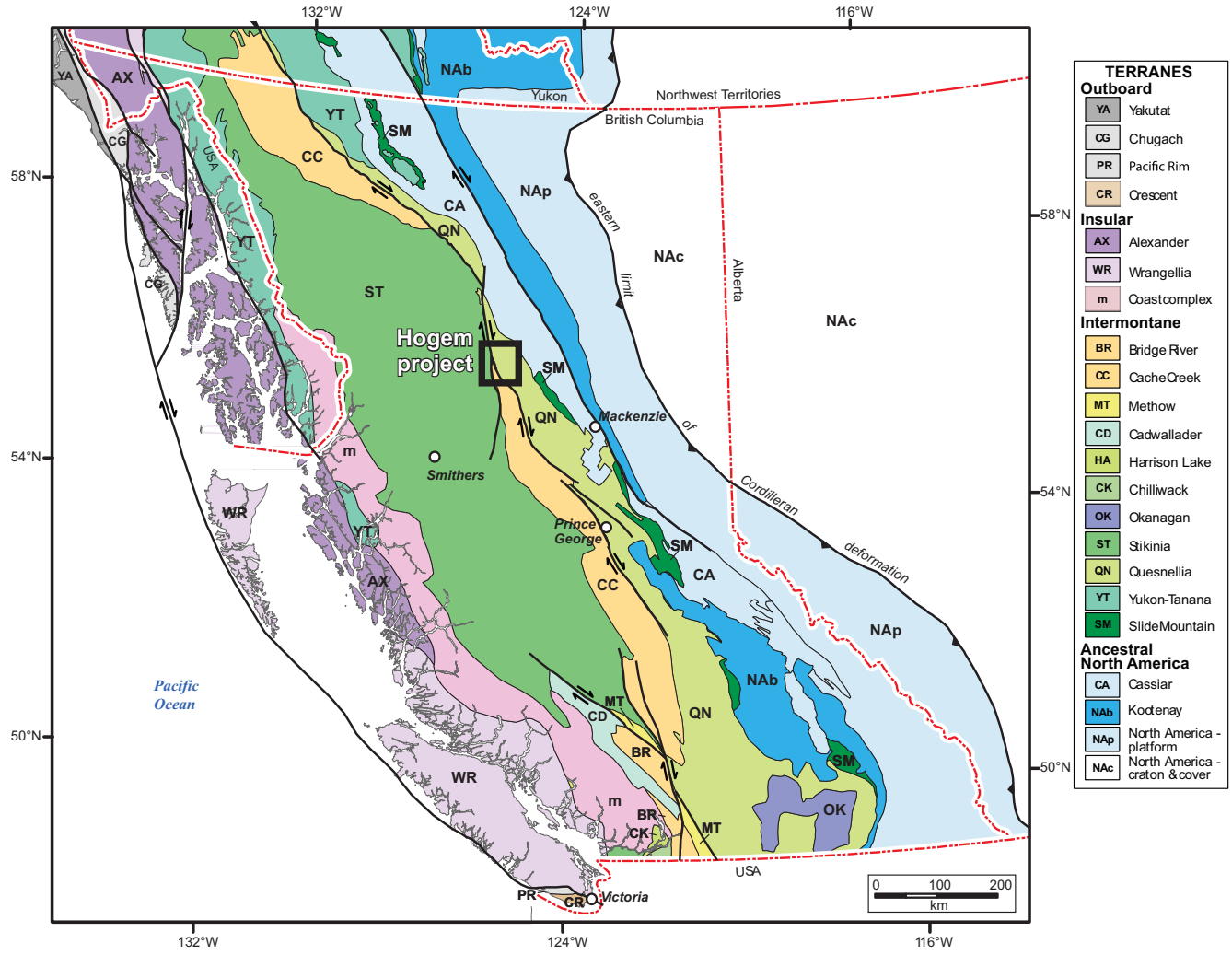

Fig. 1. Terrane map of British Columbia with location of study area. Modified after Nelson et al. (2013).

west, Stikine rocks are covered or are in fault contact with Bowser Lake and Sustut group sedimentary rocks (Jurassic to Cretaceous; Evenchick et al., 2007). CGG Canada Services Ltd. (2018) presented the results of an airborne geophysical survey that extends across much of the study area and includes both radiometric (K, U, Th) and magnetic data.

3. Quesnel terrane supracrustal rocks and northern Hogem batholith

Northern Hogem batholith was mapped by Armstrong (1946), Lord (1948, 1949), Armstrong and Roots (1948, 1954) and Roots (1954). Although Roots (1954) gave thorough descriptions of a wide variety of intrusive units, he grouped these units as 'undivided'. Woodsworth (1976) further subdivided northern Hogem batholith, and Irvine (1976) investigated ultramafic intrusions near northern Hogem batholith. In the south-central part of the study area, Nelson et al. (2003) updated mapping near the Hawk quartz vein-hosted gold prospect. Southern Hogem batholith was subdivided by Garnett (1972, 1978). Nixon and Peatfield (2003), Bath et al. (2014), and Devine et al. (2014) studied the Lorraine porphyry Cu-Au deposit southeast of the study area, providing isotopic ages for mineralization and the host rocks. Mapping by Ferri et al. (2001a, b), in areas to the east and northeast, focussed on the Takla Group (referred to herein as the Nicola Group; see below) and left the Hogem batholith largely undivided. Schiarizza and Tan (2005a, b) mapped the Nicola Group north of the study area, plotting preliminary isotopic ages for plutonic rocks at the northern tip of Hogem batholith.

3.1. Nicola Group (also referred to as Takla Group)

Previous mappers in the study area and in the general region used the term 'Takla Group' to refer to Triassic volcanic and sedimentary rocks of the Quesnel terrane (e.g., Armstrong, 1948; Lord, 1948, 1949; Armstrong and Roots, 1948; Monger, 1977; Ferri et al., 2001a, b; Schiarizza and Tan, 2005a, b). However, equivalent rocks in southern Quesnel terrane are referred to as 'Nicola Group' (see summaries in e.g., Schiarizza, 2016, 2019), which is the term we adopt here; for use in the Stikine terrane we retain 'Takla Group' (see section 4.2.). Ferri

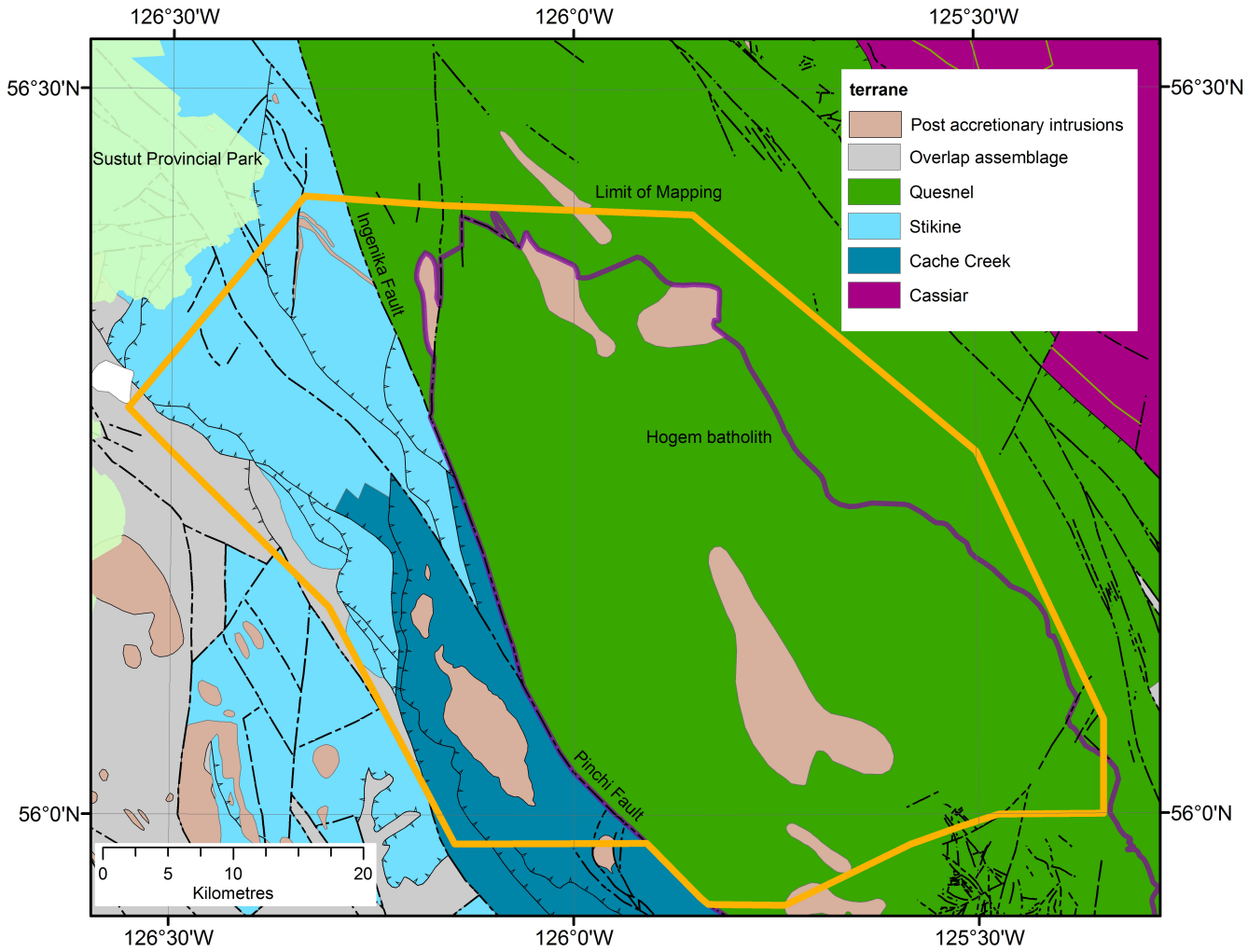

Fig. 2. Regional context of northern Hogem batholith and its surroundings. Orange line delimits the study area mapped during the 2018-2019 field seasons. Hogem batholith (purple outline) is in the Quesnel terrane, which is separated from the Cache Creek and Stikine terranes by the Pinchi-Ingenika fault (dextral strike-slip). Thrust faults on the map have teeth on the hanging wall side; dashed lines are undifferentiated strike-slip and normal faults.

et al. (2001a, b) divided these rocks into the Plughat Mountain (Late Triassic) and Vega Creek successions (Late Triassic-Early Jurassic). Only the Plughat Mountain succession is in the study area, where it consists of grey and green augite and augite-plagioclase phyric mafic tuffs and volcanic breccias with lesser volcanic flows, tuffaceous sedimentary rocks, argillites, and limestones. To the west and north, Schiarizza and Tan (2005a, b) divided the Nicola Group into the Goldway Peak unit, which consists mainly of pyroxene-bearing volcanic rocks, and the Kliyul unit, which consists mainly of volcaniclastic rocks. Both units are considered equivalent to the Plughat Mountain succession of Ferri et al. (2001a, b).

3.2. Hogem batholith

We organize the intrusive phases in northern Hogem batholith into four suites (Fig. 3) modified after Woodsworth (1976) and Woodsworth et al. (1991). The descriptions are modified and simplified from Ootes et al. (2019b). All major intrusive phases in Hogem batholith are deformed.

3.2.1. Thane Creek suite; Early Jurassic, ca. 197 to 196 Ma

The eastern and southwestern parts of the study area are underlain by diorite to quartz monzodiorite and lesser hornblendite of the Thane Creek suite, the oldest intrusive rocks in Hogem batholith (Ootes et al., 2019a, b). Diorite crosscuts and co-mingles with the hornblendite and where co-mingling is present, the rocks are texturally and compositionally heterogeneous in terms of amphibole, plagioclase, and magnetite concentrations. The diorite contains a penetrative ductile fabric defined by aligned hornblende and/or biotite. A hornblendite sample yielded a U-Pb zircon age of 197.55 ±0.11 Ma and a diorite sample yielded a $^{206}Pb/^{238}U$ zircon age of 196.61 ±0.19, both of which we interpreted as crystallization ages (see below). Biotite and hornblende from the diorite sample were also analyzed by laser step heating, yielding $^{40}Ar/^{39}Ar$ age ages of ca. 124 Ma, which we interpret to record the time of cooling through closure temperatures after regional deformation (see below).

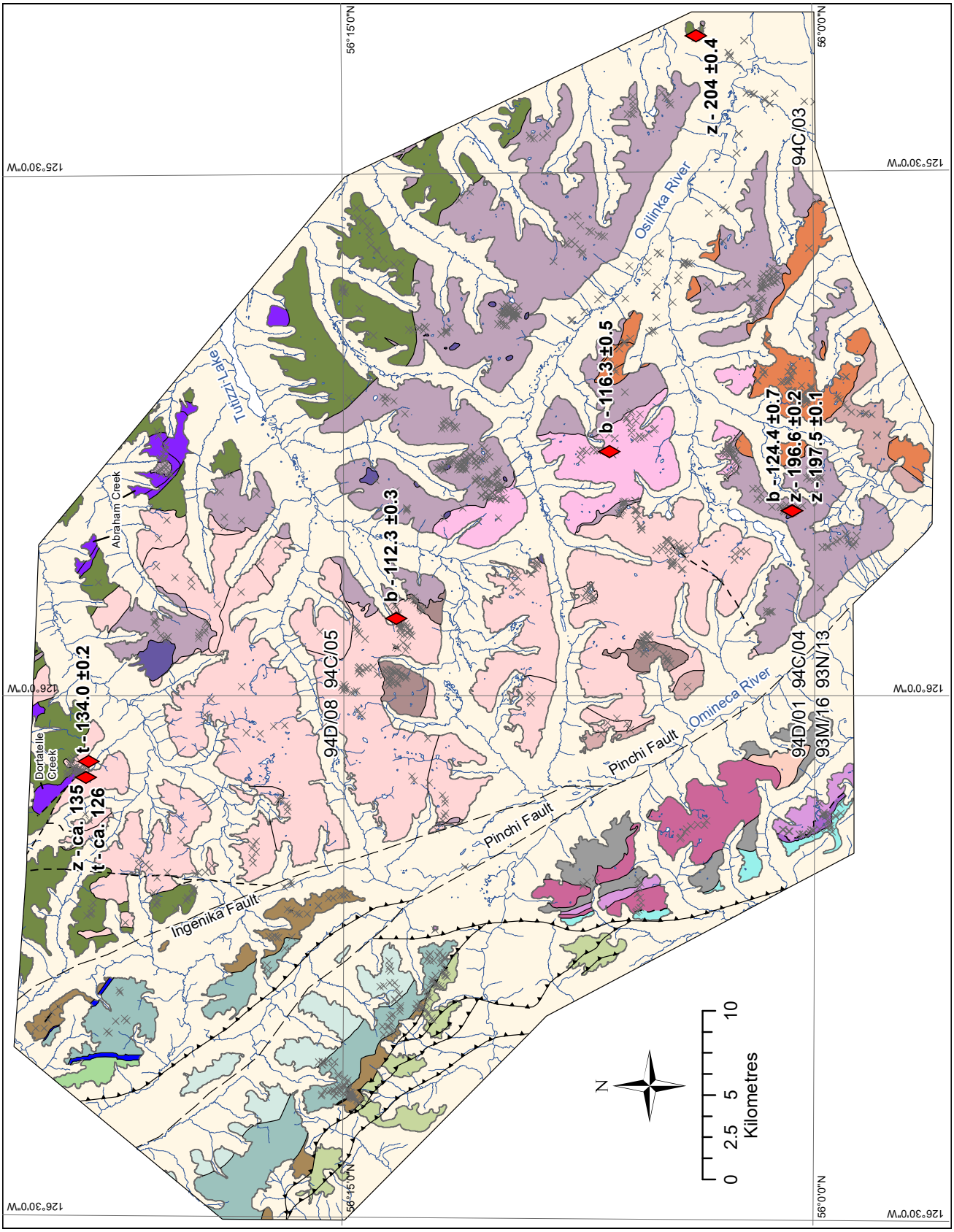

Fig. 3. Geology of northern Hogem batholith and surroundings, generalized from Ootes et al. (2020a) and modified after Lord (1949), Armstrong and Roots (1954), Richards (1976), Woodsworth (1976), Ferri et al. (2001a, b), Schiarizza and Tan (2005b), and Evenchick et al. (2007). Geochronologic data include results from this study, Mortensen et al. (1995), Schiarizza and Tan (2005b), and Ootes et al. (2020b).

Quaternary

Colluvium, alluvium and glacial drift

Overlap Assemblage

Bowser Lake and Sustut groups (may include Hazelton Group) (Upper Jurassic to Upper Cretaceous)

Undivided sedimentary and lesser volcanic rocks

Stikine Terrane

Gabbro intrusions, undivided

Hazelton Group (Lower Jurassic)

Telkwa Formation; phyllite, conglomerate, and minor sandstone (≤ 182 Ma)

Takla Group (Upper Triassic)

Moosevale or Savage Mountain Formation; andesitic and basaltic volcanic conglomerate, pyroclastic rocks, and mafic flows

Dewar Formation; sandstone, conglomerate, argillite, and slate

Asitka Group (Carboniferous to Permian)

Phyllite, argillite, slate, limestone, dolostone, chert, quartz pebble conglomerate, and felsic and mafic-intermediate pyroclastic rocks (≤ 310 Ma)

Cache Creek Terrane

Axelgold intrusive complex (Early Cretaceous)

Olivine gabbro, two-pyroxene gabbro, and anorthosite

Black Lake intrusive suite (Early Jurassic)

Granite to granodiorite

relationship unknown

Gabbro to diorite

Sitlika Assemblage (Lower Jurassic)

Undivided metavolcanic and metasedimentary rocks (≤ 200 Ma)

Sowchea succession (Upper Pennsylvanian to Lower Jurassic)

Mixed metasedimentary and metavolcanics rocks

Trembleur ultramafite (Permian to Upper Triassic)

Ultramafic rocks

Quesnel Terrane

Hogem batholith (Jurassic to Cretaceous)

Mesilinka suite

Undivided equigranular and K-feldspar porphyritic granite (ca. 135 Ma)

Granodiorite to quartz monzonite (ca. 140 Ma)

Tonalite (ca. 174 Ma)

Osilinka suite

Equigranular granite with low mafic mineral content (ca. 160 Ma)

Duckling Creek suite

Undivided biotite pyroxenite and monzonite to syenite (182 to 178 Ma)

Thane Creek suite

Diorite to quartz monzodiorite, monzodiorite, and minor gabbro (ca. 197 Ma)

Hornblendite (ca. 198 Ma)

Mafic to ultramafic intrusive complex (Late Triassic to Early Jurassic)

Undivided ultramafic rocks, Abraham Creek and Dortatelle Creek

Nicola Group (Upper Triassic)

Plughat Mountain successsion

Undivided mafic volcanic and lesser sedimentary rocks

Field station

Geochronological sample: b = Ar/Ar biotite; z = U/Pb zircon

Contact

Fault undifferentiated

Thrust Fault

Fig. 3. Continued.

3.2.2. Duckling Creek suite; Early Jurassic, ca. 182 to 178 Ma

The south-southeast part of the study area is underlain by quartz-undersaturated rocks of the Duckling Creek suite (Fig. 3). South of the study area, Devine et al. (2014) identified three stages of the Duckling Creek suite and constrained the timing with U-Pb zircon ages: 1) biotite pyroxenite (ca. 182 to 178.5 Ma); 2) predominantly K-feldspar porphyritic syenite to monzonite (ca. 178.8 to 178.4 Ma); and 3) massive syenite and pegmatite (ca. 177 to 175 Ma). All three phases exist in the study area. The oldest phase is biotite pyroxenite, locally with megascopic phenocrysts (up to 0.5 cm) of white weathering apatite. Biotite pyroxenite is crosscut by syenite to monzonite, with lesser monzodiorite. These rocks range from equigranular to porphyritic to pegmatitic. Porphyritic varieties contain tabular, commonly zoned, K-feldspar phenocrysts (up to 5 cm long) that are set in a groundmass of equigranular green pyroxene and lesser plagioclase (possibly albite), hornblende, magnetite, titanite, and apatite. Rhythmic magmatic layering defined by varying felsic and mafic mineral ratios and alignment of K-feldspar phenocrysts is common. The entire unit has moderate to strong magnetism, with areas of highest magnetism spatially associated with biotite pyroxenite. The biotite pyroxenite zones are locally stained with malachite and have disseminated chalcopyrite.

Hornblende was separated from a K-feldspar porphyritic syenite sample and analyzed by laser step-heating, yielding an integrated $^{40}Ar/^{39}Ar$ age of a ca. 177.6 Ma (Ootes et al., 2020b). This result overlaps, within uncertainty, with a previously reported $^{40}Ar/^{39}Ar$ biotite age of 177.1 ±0.9 Ma for a similar syenite sample to the south (Devine et al., 2014). These ages are best interpreted as magmatic cooling through the closure temperature of hornblende (ca. 550°C).

3.2.3. Osilinka suite; Late Jurassic, ca. 160 Ma

The central part of the Hogem batholith is underlain by a unit of mafic-poor equigranular granite of the Osilinka suite. The scarcity of micaceous or mafic minerals in the granite likely hampered the development of a foliation and the granites appear massive, but mafic dykes within it contain penetrative foliation and shear fabrics (Ootes et al., 2019b).

Preliminary geochemical results indicate that this unit is an S-type granite and preliminary geochronology indicate that it contains significant zircon inherited from older crustal sources; the youngest zircons are ca. 160 Ma, providing a maximum crystallization age for the granite (Ootes et al., 2020b). This granite was previously thought to be the youngest mappable intrusive phase in Hogem batholith (Ootes et al., 2019a, b), but is now considered older than the granitic rocks of the Mesilinka suite (section 3.2.4.). Biotite and muscovite from an Osilinka granite sample were analyzed by laser step heating, yielding $^{40}Ar/^{39}Ar$ cooling ages between ca. 122 to 115 Ma (see below). These cooling ages are interpreted to post-date the peak of regional deformation.

3.2.4. Mesilinka suite; Early Cretaceous, ca. 140 Ma, but with mappable Middle Jurassic, ca. 174 Ma, enclaves

Throughout the western part of the study area the predominant rock type is equigranular and K-feldspar porphyritic granite (Fig. 3). These rocks contain elevated Th over K and are particularly evident on the Th/K radiometric maps (CGG Canada Services Ltd, 2018; Ootes et al., 2019a). The K-feldspar porphyritic granite crosscuts the equigranular granite and both contain a foliation that cuts the intrusive contacts. Both contain enclaves of tonalite and granodiorite. The tonalite enclaves form small mappable bodies in the western part of the study area (Fig. 3), and we previously considered them be part of the Thane Creek suite (Ootes et al., 2019a, b). However, the tonalite only occurs as enclaves within the younger Mesilinka granites and Schiarizza and Tan (2005b) reported a preliminary age of ca. 174 Ma age for similar tonalites in northern Hogem batholith. Thus, we now consider the tonalite as the oldest phase of the Mesilinka suite. Similarly, we now consider that the granodiorite enclaves in the southwest part of Hogem batholith that we previously assigned to Thane Creek suite (Ootes et al., 2019a, b) are part of the Mesilinka suite. In addition, preliminary geochemical data (Ootes et al., 2020b) indicate that these granodiorites have a kinship with their granitic hosts.

The Mesilinka granites are S-type and preliminary U-Pb zircon results indicate significant inheritance from older crustal sources, with the youngest zircons (ca. 135 Ma) providing a maximum crystallization age (Ootes et al., 2020b). Biotite from a Mesilinka K-feldspar porphyritic granite sample yielded an integrated $^{40}Ar/^{39}Ar$ age of 112.3 ±0.3 Ma (see below) and two separate aliquots of biotite from a tonalite sample yielded $^{40}Ar/^{39}Ar$ ages of ca. 112 and 109 Ma ages (Ootes et al., 2020b), which we consider related to post-deformation uplift. However, mineral separates from a granodiorite phase yielded an $^{40}Ar/^{39}Ar$ age for biotite of ca. 122.6 Ma and for hornblende of ca. 139 Ma (Ootes et al., 2020b), potentially indicating primary magmatic cooling before deformation.

3.3. Mafic-ultramafic intrusive complexes; Late Triassic to Early Jurassic

Mafic-ultramafic intrusive complexes are on the periphery of northern Hogem batholith and surrounding Nicola Group (Fig. 3; e.g., Irvine, 1976; Ferri et al., 2001a). They differ from the Thane Creek suite hornblendites by containing olivine and clinopyroxene-rich ultramafic rock types. The precise age of the mafic-ultramafic complexes remains unknown but are considered Late Triassic to Early Jurassic.

3.3.1. Abraham Creek intrusive complex

The Abraham Creek intrusive complex is an elongate (ca. 30 by 5 km) northeast-trending body that cuts the Nicola Group northeast of the Hogem batholith (Fig. 3; Ferri et al., 1993, 2001a). Also known as the Aiken Lake intrusive complex (Massey et al., 2005a, b), it consists of hornblende gabbro, diorite, and clinopyroxenite with lesser peridotite, hornblendite, and orthopyroxenite (Irvine, 1976; Ferri et al., 1993). The

complex displays a strong aeromagnetic signature that contrasts with the weak to moderately magnetic host rocks. The most mafic rock type is dark grey-green, medium-grained olivine (<25%) clinopyroxenite (Fig. 4a) that is magnetite bearing and serpentinized. This grades into magnetite-hornblende clinopyroxenite with saussuritized interstitial plagioclase. Ubiquitous igneous breccias include fragments of dark green clinopyroxenite in a hornblende-rich gabbro to diorite groundmass (Fig. 4b). Northwest-striking, shallowly dipping, <30 cm wide quartz veins are associated with narrow (ca. 1 m) zones of rusty-weathering, malachite-stained clinopyroxenite, indicating local Cu-sulphide mineralization.

3.3.2. Dortatelle Creek ultramafic complex

The Dortatelle Creek ultramafic complex (Lord,1948; Irvine, 1976; Schiarizza and Tan, 2005b) is an elongate, northwest-trending ultramafic body in the northernmost part of the map area (Fig. 3). Its high aeromagnetic expression (CGG Canada Services Ltd., 2018) indicates dimensions of 5 by 1.5 km. The southwest flank of the complex is cut by weakly to moderately magnetic, high-Th granite of the Mesilinka suite with well-developed internal high-strain zones (Fig. 4d). To the northeast, the ultramafic rocks are in structural contact with highly strained rocks of the Nicola Group. Brown-weathering, fine- to medium-grained, fresh dunite is the predominant and most mafic lithology in the southeastern part of the complex (Fig. 4c). Trace amounts of chromite are homogeneously disseminated throughout the dunite. Dunite is crosscut by dikes of sugary, garnet±muscovite-bearing granite of the Mesilinka suite. Close to the granite are veins and stockworks of talc±carbonate. Green-weathering, variably magnetite-rich, olivine clinopyroxenite is also a main lithology.

4. Stikine terrane

Rocks assigned to the Stikine terrane in the study area were mapped by Lord (1948, 1949) and further subdivided by Richards (1976). Details of Permian (Asitka Group) and Triassic (Takla Group) units are summarized in Monger (1977) and the Jurassic section (Hazelton Group) is summarized in Tipper and Richards (1976). Evenchick et al. (2007) further refined Stikine geology focussing on Jurassic to Cretaceous overlap assemblages (e.g., Bowser Lake and Sustut groups).

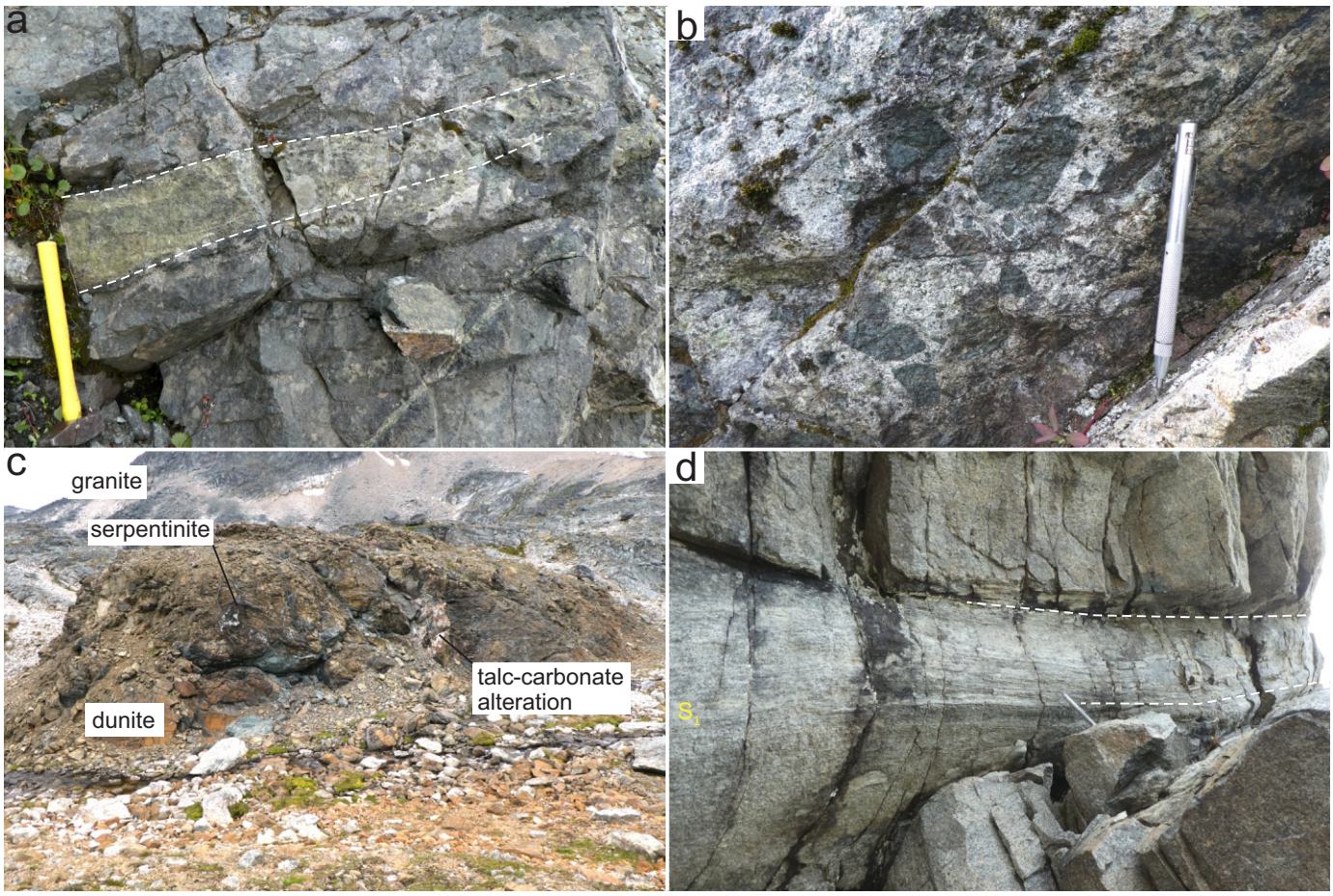

Fig. 4. a) Abraham Creek intrusive complex olivine clinopyroxenite (dark green), cut by a zone of hydrothermal epidote alteration (light green, bounded by white dashed lines). **b)** Abraham Creek intrusive complex intrusive breccia with olivine clinopyroxenite enclaves in a diorite groundmass. **c)** Dortatelle ultramafic complex rocks. Mesilinka suite granitic rocks are in the background. **d)** A high-strain zone (bounded by white dashed lines) in a strongly foliated, biotite-rich, equigranular granite of the Mesilinka suite.

4.1. Asitka Group

The Asitka Group (Carboniferous to Permian) represents a basement domain to the Stikine terrane. It is composed of felsic to intermediate flows and tuffs, argillites, slates, limestones, dolostones, and cherts (Fig. 5; Lord, 1948, 1949; Monger, 1977). A minimum thickness is estimated to be 2600 m, but the base is not exposed (Lord, 1948). Fossils, including fusulinids, corals, brachiopods, and bryozoan indicate it was deposited in the Lower Permian (Lord, 1948, 1949; Monger, 1977). Diakow (2001) reported a ca. 308 Ma U-Pb zircon crystallization age from a rhyolite about 80 km north of the study area. Although it was considered part of the Asitka Group, this rhyolite may be part of an older Carboniferous basement to the Stikine terrane (L. Diakow, personal communication 2019). Uranium-lead detrital zircon results from a quartz pebble conglomerate sample indicate provenance from Carboniferous sources, with the youngest zircons at ca. 310 Ma (Ootes et al., 2020b). Paleomagnetic data, acquired from volcanic rocks of the Asitka Group, indicate deposition at paleolatitudes of 21° to 23° N (Irving and Monger, 1987).

The Asitka Group underwent low-grade metamorphism and deformation, and many of the fine-grained siliciclastic units are best described as phyllites with a bedding-parallel foliation. Bedding (S_0) is best preserved in the chert units, where interbedded brown mudstone and chert are readily identifiable (Fig. 5b). In the phyllites and slates, bedding is transposed into a subparallel foliation (S_0 - S_1; Figs. 5c, d). Second generation structures are locally preserved as folds of S_0-S_1 and as a rare spaced crenulation cleavage (S_2; Figs. 5c, d). Second generation fold axes are moderately plunging, generally to the north-northeast. In the same outcrop however, the azimuth of fold axes in different folds can vary up to 90° (Fig. 6a), which may indicate that these folds are refolded.

4.2. Takla Group; Dewar Formation

The Asitka Group is unconformably overlain by the Takla Group (Fig. 3; Triassic; Lord, 1948; Monger, 1977). The basal unit of the Takla Group is the Dewar Formation, which comprises interbedded sandstone, siltstone, and argillite (Fig. 7). The Savage Mountain Formation is composed of mafic

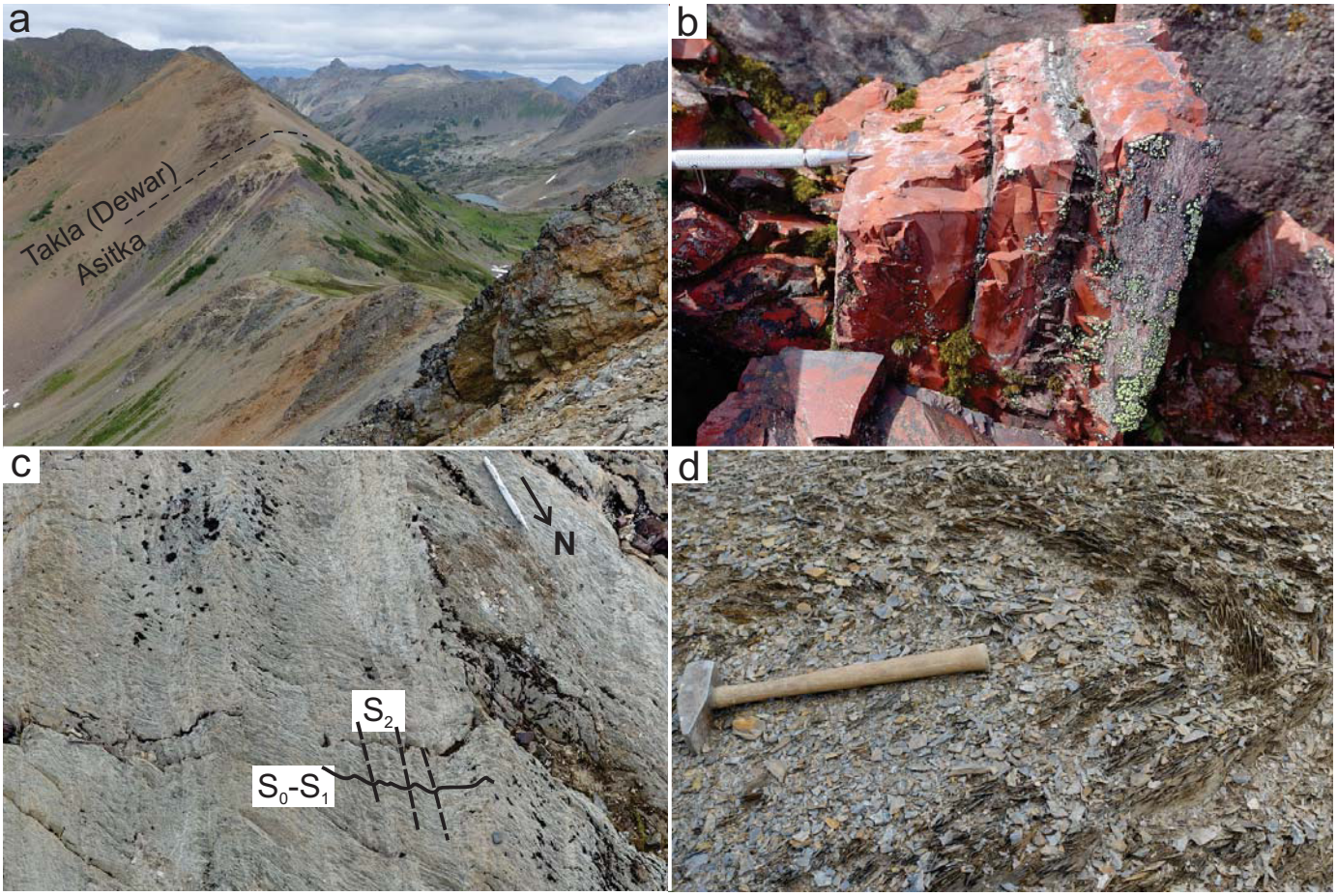

Fig. 5. Representative outcrop photographs of the Asitka Group. **a)** View looking up-section, showing the variable weathering colours of this unit. The resistant weathering outcrop in the immediate foreground (bottom right) is either feldspathic sandstone or felsic-intermediate volcanic flow. The upper contact with the Dewar Formation of the Takla Group is estimated. Photograph is from the western-most part of the study area, and the view is toward the northeast. **b)** Red-weathering chert with brown mudstone interbeds. **c)** Relationship between bedding and bedding parallel foliation (S_0-S_1) and a weakly developed spaced crenulation cleavage (S_2) in phyllite. **d)** Steeply northeast plunging F_2 fold of slaty bedding and cleavage.

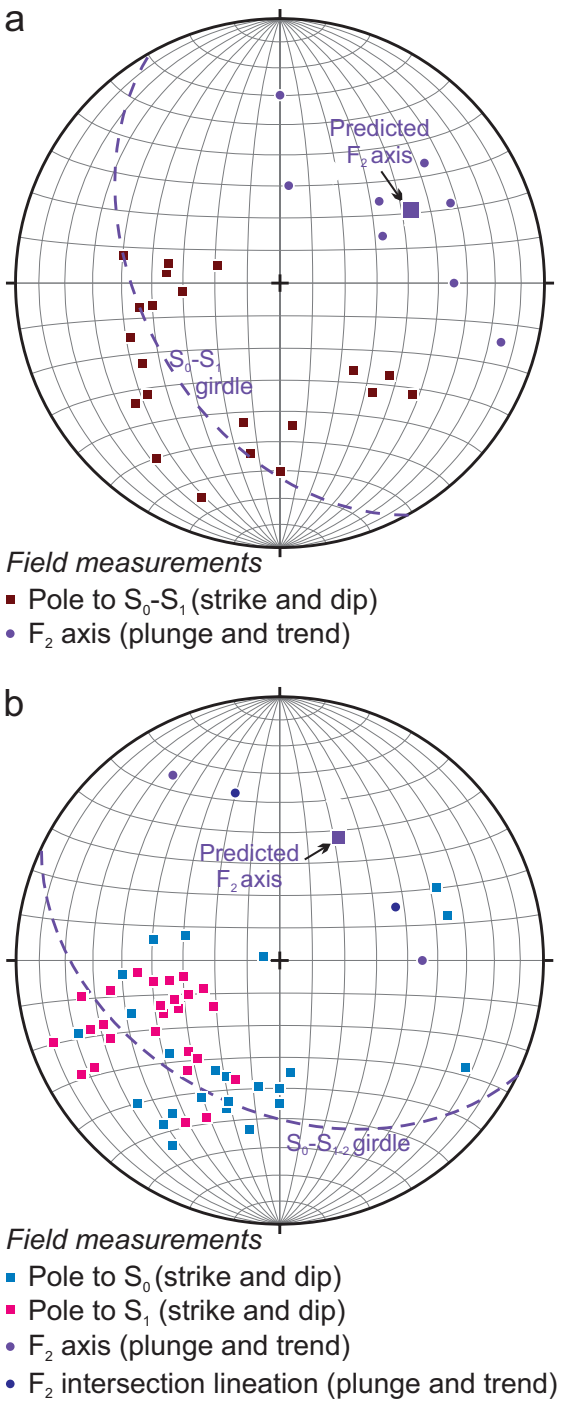

Fig. 6. Equal area stereonet lower hemisphere projections. **a)** Poles to Asitka Group bedding and bedding parallel foliation (S_0-S_1) define a best-fit great circle (S_0-S_1 girdle) with a pole that should predict the F_2 fold axis (purple square). **b)** Dewar Formation (Takla Group) and Telkwa Formation (Hazelton Group) structural measurements showing the same relationships as those depicted in a), but with S_0 and S_1 separated. Plots generated using Allmendinger software, available at: http://www.geo.cornell.edu/geology/faculty/RWA/programs/stereonet.html.

flows and pyroclastic rocks and overlies and is intercalated with the Dewar Formation. The uppermost Moosevale Formation is mostly coarse-grained volcaniclastic rocks (Monger, 1977). The Dewar Formation was examined at one location in the study area, where black, graphitic shale (slate) is above steel-grey phyllite and brown carbonate rocks of the Asitka Group (Fig. 7a). These rocks grade upsection into slate, then into thick-bedded (up to 1.5 m) feldspathic sandstone (±grains of clinopyroxene) with interbeds of argillite and lesser slate (Figs. 7a-c). Local cross beds in the sandstones and load casts and flame structures at sandstone-argillite contacts (Fig. 7b), indicate that bedding is upright and youngs to the east. Deformation in the Dewar Formation is similar to that of the Asitka Group and displayed as foliations that are sub-parallel to bedding and interpreted as S_1, and folds that are interpreted as F_2 (Fig. 6b).

4.3. Hazelton Group (latest Triassic to Middle Jurassic), Telkwa Formation

The Takla Group is overlain by the Hazelton Group. In the present map area, it includes three formations, from base to top: Telkwa, Nilkitkwa, and Smithers (Tipper and Richards, 1976; Monger, 1977). The Telkwa Formation is the main unit exposed in the study area (Fig. 3), although Evenchick et al. (2007) included other undivided Hazelton Group units. The Telkwa Formation consists of volcanic-derived siliciclastic rocks that are difficult to distinguish from the Moosevale Formation of the Takla Group, and commonly have similar weathering colours (maroon and green) to the Asitka Group (Monger, 1977). It includes clast-supported, monomictic (feldspar porphyry clasts) and polymictic (volcanic clasts) cobble conglomerates that are interbedded with purple well-sorted feldspathic sandstones, and purple, maroon, and green shales (Fig. 7d). Upsection are monomictic pebble conglomerates with intermediate volcanic clasts (Fig. 7e). Uranium-lead detrital zircon results from a volcanic-pebble conglomerate sample indicate provenance from Upper Triassic and Lower Jurassic sources, with the youngest zircons at ca. 182 Ma (Ootes et al., 2020b).

4.4. Overlap assemblages: Bowser Lake and Sustut groups

In the west-southwest part of the study area, the Bowser Lake (Jurassic-Cretaceous) and Sustut (Cretaceous) groups were mapped by Evenchick et al. (2007). These are undivided on Figure 3 where they are depicted in thrust contact with the structurally overlying Telkwa Formation and undivided Hazelton Group rocks and locally against the Asitka Group (Fig. 7a; Evenchick et al., 2007).

5. Cache Creek terrane

Rocks assigned to the Cache Creek terrane were mapped by Lord (1948, 1949) and further subdivided by Monger (1974), Paterson (1974), and Richards (1976), and Irvine (1974, 1976) mapped the Axelgold layered mafic intrusion. Immediately

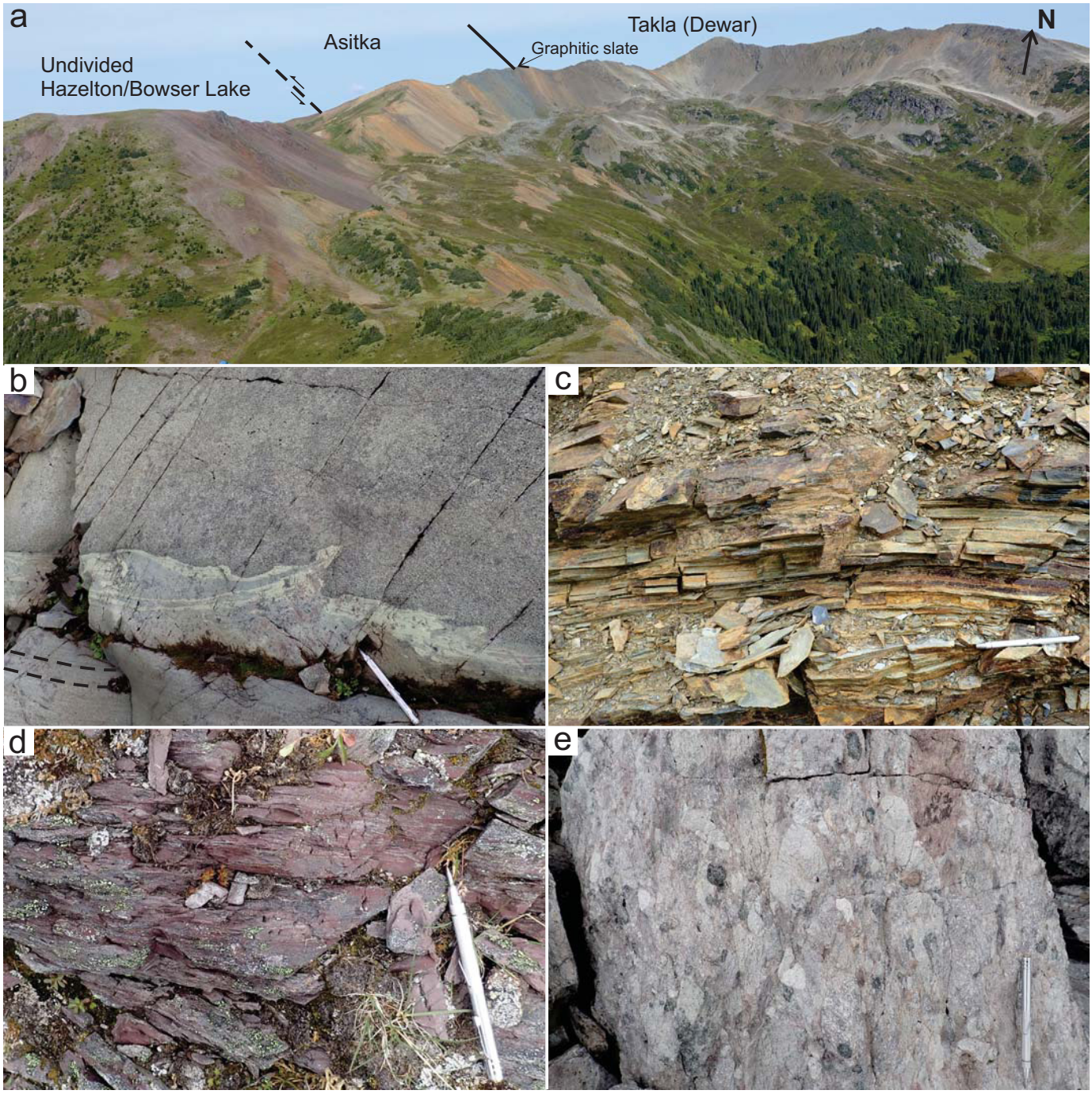

Fig. 7. Outcrop photographs of the Hazelton and Bowser Lake groups, Dewar Formation (Takla Group) and Telkwa Formation (Hazelton Group). **a)** A section of undivided Hazelton Group and Bowser Lake Group purple volcanic rocks that contain copper mineralization is structurally beneath the Asitka Group, which is overlain by the Dewar Formation, the base of which is marked by graphitic slates. View is to the north. **b)** Dewar Formation massive grey feldspathic cross-stratified sandstone with interbedded, fine-grained, green-grey argillite displaying flame structures. Beds are upright, younging is toward the top of the photograph. Dashed black lines mark subtle cross-beds in the lower sandstone bed. **c)** Dewar Formation slate. **d)** Telkwa Formation maroon mudstone. **e)** Telkwa Formation polymictic cobble conglomerate with volcanic clasts.

south of the study area, rocks of the Cache Creek terrane were mapped by Schiarizza (2000) and Evenchick et al. (2008).

5.1. Sowchea succession

The Sowchea succession (Upper Pennsylvanian to Upper Triassic; also referred to as Cache Creek Group; Paterson, 1974; Richards, 1976; Evenchick et al., 2007) includes phyllite chert, marble, greywacke, greenstone, amphibolite, and chlorite schist (Paterson, 1974; Schiarizza, 2000). A high-temperature contact metamorphic aureole is present around the Axelgold layered intrusion (Irvine, 1974).

5.2. Trembleur ultramafite serpentinite

Pervasively serpentinized ultramafic rocks form a narrow and discontinuous northwest-striking belt at least 25 km long, which follows the general structural and geophysical fabric of the area west of the Pinchi fault. The serpentinite weathers yellow-brown to dark brown and is dark green to dark grey on fresh surfaces. Warty textures on weathered surfaces indicate a harzburgitic or lherzolitic protolith that has been recrystallized to serpentine and magnetite±brucite, magnesite. Locally, metamorphic olivine and clinopyroxene indicate prograde metamorphism of serpentinite. In serpentine breccias, rounded fragments of light-weathering, medium-grained, massive serpentinite float in a darker, red and brown-weathering, fine-grained, foliated serpentinite matrix (Fig. 8a). The serpentinite has a high magnetic expression on the regional aeromagnetic map (CGG Canada Services Ltd., 2018). Sulphides are present in trace amounts in the serpentinized rocks.

In the southwest corner of the study area, strongly serpentinized peridotite is bordered to the west by gabbro to diorite of uncertain affinity. Near the contact, slivers of highly serpentinized rocks (Fig. 8b) may represent rafts of peridotite in diorite or fault slices.

5.3. Sitlika assemblage

The Sitlika assemblage (Upper Triassic to Lower Jurassic; Paterson, 1974) includes fine- to medium-grained, moderately to strongly foliated, greenschist-facies volcanic and sedimentary rocks. These rocks generally have a low to moderate aeromagnetic signature. In the southwest corner of the study area the unit forms two principal lithologic belts (Fig. 3). The western belt includes fine-grained brown to rusty argillaceous schist and medium-grained, calcareous clinozoisite-muscovite-biotite-quartz schist that are northwest-striking and moderately to steeply northeast dipping. The clinozoisite occurs as porphyroblasts that have corroded margins and are aligned along a muscovite and biotite-defined foliation (Fig. 8c). The eastern belt consists of fine-grained light green- to grey-weathering, moderately to strongly foliated chlorite-sericite schist that may have a volcanic protolith, similar to rocks interpreted by Logan et al. (2010) to have been derived from mafic to intermediate volcanic rocks. Locally, subparallel bedding and schistosity in argillaceous schists define broad open, nearly recumbent gently westward plunging folds (Fig. 8d). Paterson (1974) considered the age of the Sitlkika assemblage to be Upper to Triassic to Jurassic. Outside the study area, the Sitlika assemblage

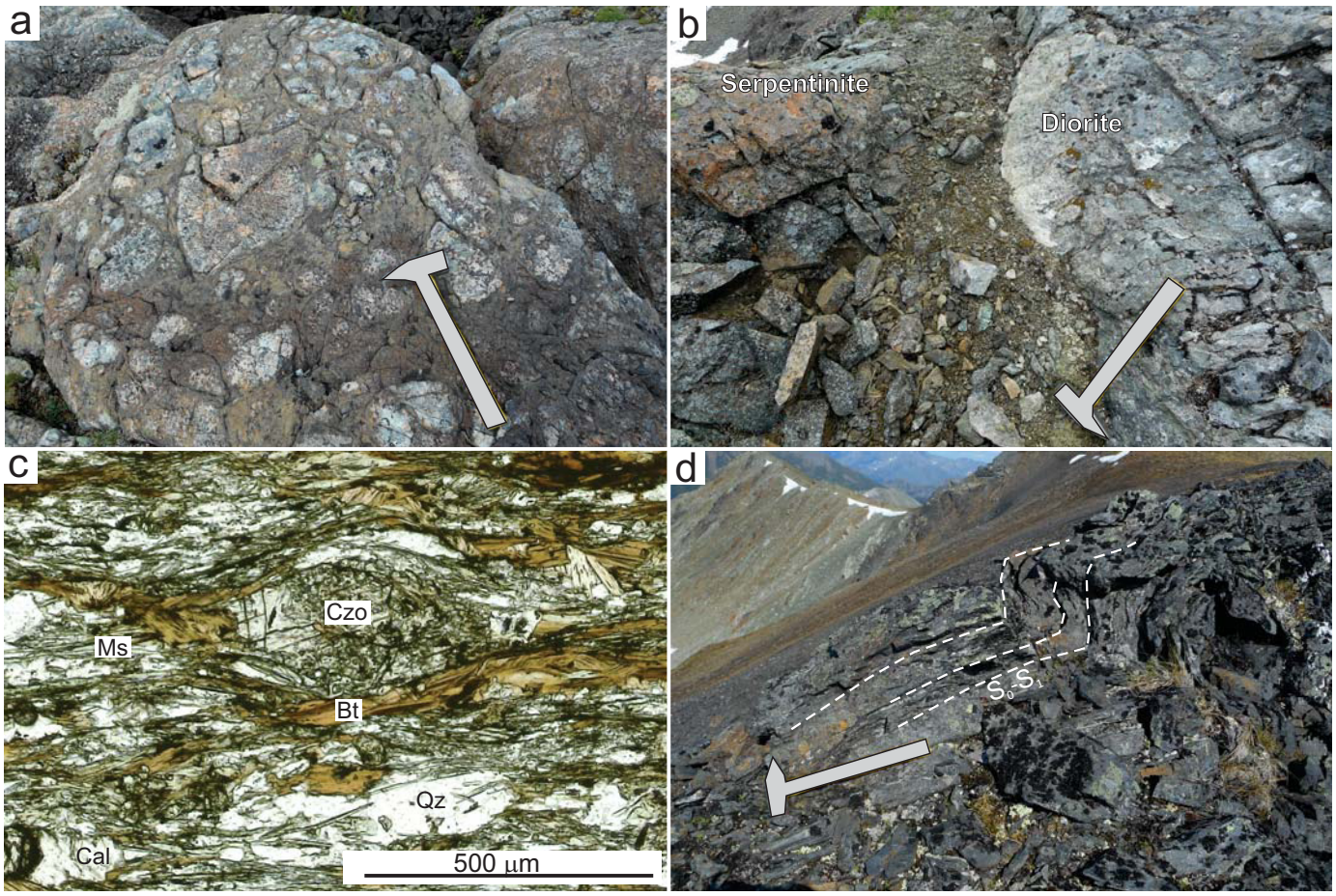

Fig. 8. a) Trembleur ultramafite serpentinite breccia. **b)** Trembleur ultramafite serpentinite adjacent to diorite (gabbro-diorite unit). **c)** Plane-polarized light photomicrograph of a strongly foliated (S_1), calcareous clinozoisite-muscovite-biotite-quartz schist from the western belt of the Sitlika assemblage. Bt=biotite; Cal=calcite; Czo=clinozoisite; Ms=muscovite; Qz=quartz. **d)** Sitlika assemblage argillaceous schists with broad open fold of subparallel bedding (S_0) and schistosity (S_1); hinge line plunges 20° toward 270°.

is considered to be Permian-Jurassic (Logan et al., 2010). Uranium-lead detrital zircon results from a sandstone sample indicate provenance from Carboniferous and Triassic sources, with the youngest zircons at ca. 200 Ma (Ootes et al., 2020b).

5.4. Gabbro to diorite

In the southwest part of the map area, mafic to intermediate intrusive rocks outcrop in a narrow sliver bounded by on the southwest by the Sitlika assemblage and the northeast by Trembleur ultramafic rocks. They display a mottled appearance defined by variable abundance and coarseness of the main minerals, plagioclase and hornblende. Other phases include apatite, alkali feldspar, quartz, and epidote. Fine-grained, sugary-textured, foliated intermediate to felsic quartz and/or feldspar phyric hypabyssal intrusive rocks are ubiquitous. Centimetre to metre-scale screens of well foliated Sitlika assemblage chlorite-sericite schist are in the intrusion, but the intrusive rocks lack a penetrative foliation and are considered to have intruded after development of the foliation.

5.5. Black Lake intrusive suite (Early Jurassic)

Cache Creek terrane rocks are cut by biotite-hornblende bearing granite to granodiorite that are assigned to the Black Lake intrusive suite (Jurassic; Evenchick et al., 2007). Only one pluton of this suite is in the study area (Fig. 3; Evenchick et al., 2007).

5.6. Axelgold layered gabbro intrusion (Early Cretaceous)

Rocks of the Axelgold intrusion are typically coarse-grained black to brown to green white weathering olivine gabbro, two-pyroxene gabbro, and anorthosite, and include lesser syenite phases. Magmatic layering is ubiquitous at the m-scale and consists of variable gabbroic compositions; overall the layering appears define a bowl shape (Irvine, 1975, 1976). A high-temperature metamorphic aureole is preserved in the Sowchea succession rocks. The pluton is undeformed, which led Irvine (1975) to estimate it was emplaced in the Cretaceous; subsequent K-Ar and Rb-Sr dating by Armstrong et al. (1985) yielded an age of 125 ±5 Ma.

6. Geochronology

Herein we present two results of U-Pb zircon chemical abrasion isotope dilution thermal ionization mass spectrometry (CA-ID-TIMS) conducted at the Pacific Centre for Isotopic and Geochemical Research (PCIGR), Department of Earth, Ocean and Atmospheric Sciences at the University of British Columbia (Fig. 9; Table 1). Unless otherwise noted, all errors are quoted at 2s (95% level of confidence). Isotopic ages were calculated with the decay constants l_{238}=1.55125^{-10} and l_{235}=9.8485^{-10} (Jaffey et al., 1971) and a $^{238}U/^{235}U$ ratio of 137.88. Uranium-lead zircon results presented without supporting data were analyzed by split-stream laser ablation inductively coupled plasma mass spectrometry at the University of Alberta. Methods, data, and interpretations are presented in Ootes et al. (2020b). We also present selected results from $^{40}Ar/^{39}Ar$ laser step heating, which

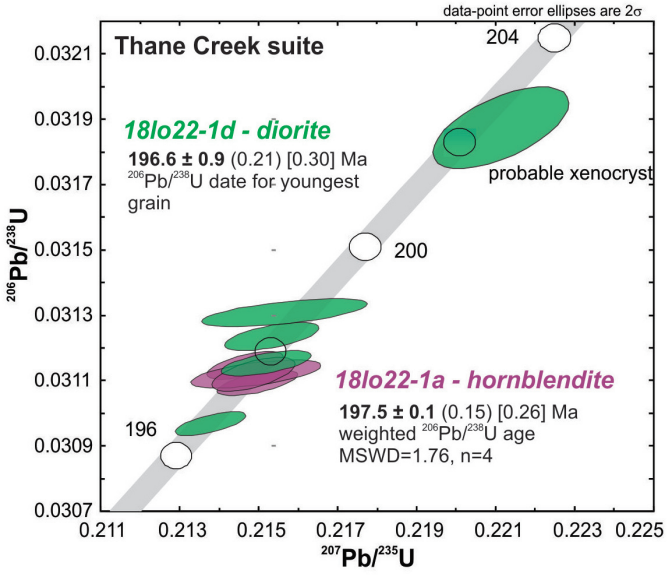

Fig. 9. Results of chemical abrasion ID-TIMS U-Pb zircon geochronology for Thane Creek diorite (18lo22-1d; green ellipses) and hornblendite (18lo22-1a; purple ellipses). MSWD=mean square of weighted deviation. Sample locations are in Figure 3, analytical results are in Table 1.

was performed at the University of Manitoba. A value of 295.5 was used for the atmospheric $^{40}Ar/^{36}Ar$ ratio (Steiger and Jaëger, 1977) and the decay constants were those recommended by Min et al. (2000). Each of the steps has relatively small errors, and the integrated ages are calculated from the average and uncertainty by standard deviation of the best analysis (Fig. 10; Table 2). Complete datasets and full methods are presented in Ootes et al. (2020b).

6.1. Thane Creek suite

6.1.1. Hornblendite sample 18lo22-1a

This sample was collected from a zone with pegmatitic plagioclase segregations in the hornblendite. It yielded good-quality igneous zircon. Four single grain zircon analyses yield concordant results that overlap within error at 197.55 ±0.11 Ma and have a narrow overlapping range of $^{206}Pb/^{238}U$ ages (Fig. 9; Table 1), interpreted as the time of crystallization of the hornblendite.

6.1.2. Diorite sample 18lo22-1d

This sample, consisting of homogeneous diorite, was collected ca. 30 m east of its intrusive contact with hornblendite of sample 18lo22-1a. It yielded good-quality igneous zircon; five single grain analyses are concordant but yield a spread of ages from ca. 202 to 196.5 Ma (Fig. 4) with a similar spread in the $^{206}Pb/^{238}U$ ages (Table 1). The youngest zircon analyzed yields a 196.61 ±0.19 $^{206}Pb/^{238}U$ age, interpreted as the time of crystallization of the diorite. The older zircons are interpreted as antecrysts or inherited (Fig. 9).

Biotite in the sample was analyzed by laser step heating. Nine release steps were conducted during the analysis. The biotite yielded an integrated $^{40}Ar/^{39}Ar$ age of 124.4 ±0.7 Ma,

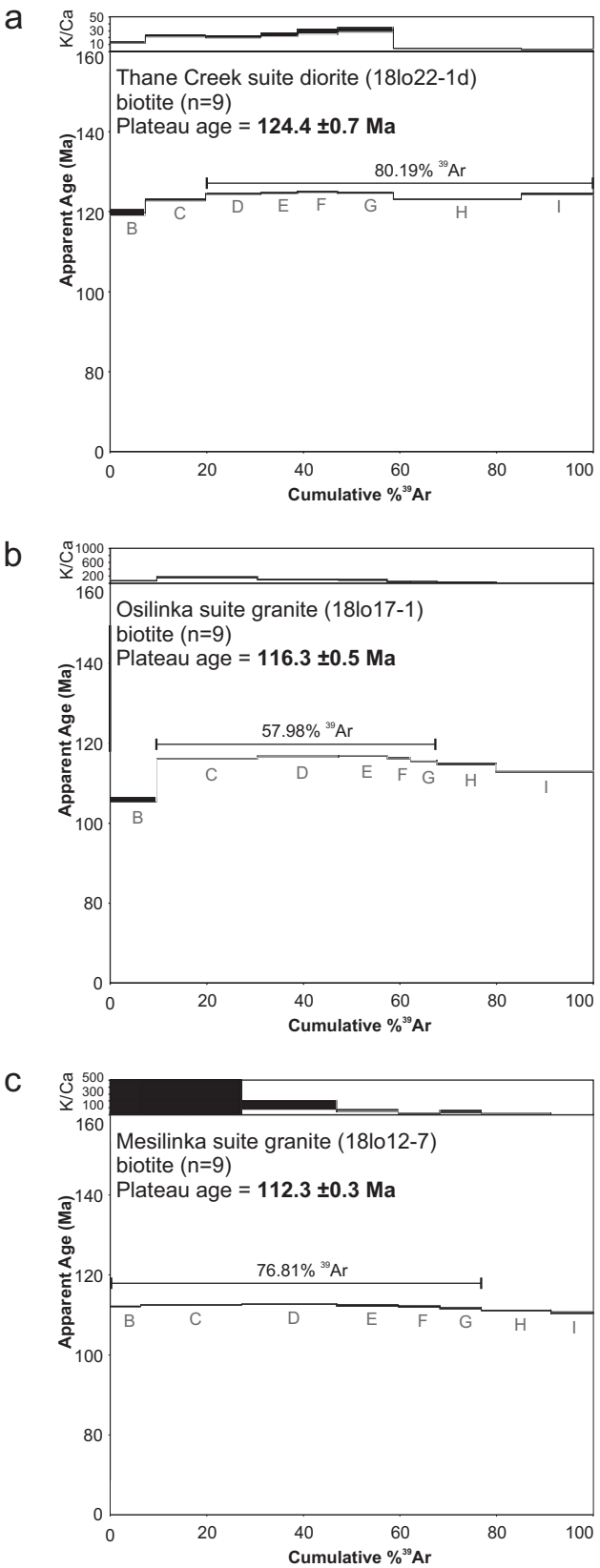

Fig. 10. Results of $^{40}Ar/^{39}Ar$ laser step heating for single biotite crystals. **a)** Thane Creek suite diorite (18lo22-1d). **b)** Osilinka suite granite (18lo17-1). **c)** Mesilinka suite K-feldspar porphyritic granite (18lo12-7). See text for description of plateau age determination.

representing 69.13% of ^{39}Ar released (steps D-I; Fig. 10a; Table 2). Hornblende was also analyzed and yielded a ca. 123 Ma integrated age (Ootes et al., 2020b). The results indicate the diorite cooled through the hornblende and biotite closure temperatures (ca. 550 to 300°C) at ca. 124 Ma, interpreted to post-date regional deformation.

6.2. Duckling Creek suite: K-feldspar porphyritic syenite

Hornblende from this sample yielded an integrated $^{40}Ar/^{39}Ar$ age of a ca. 177.6 Ma (Ootes et al., 2020b), best interpreted as a magmatic cooling age.

6.3. Osilinka suite

Many of the zircons analyzed are inherited from older crustal sources; the youngest zircons are ca. 160 Ma, providing a maximum crystallization age for the granite (Ootes et al., 2020b). Nine laser steps were conducted on biotite from an Osilinka granite sample (18lo17-1) and the results indicate a relatively well-behaved plateau, with an integrated $^{40}Ar/^{39}Ar$ age of 116.3 ±0.5 Ma, representing 57.98% of ^{39}Ar released (steps C-G; Fig. 10b; Table 2). Muscovite was also separated from the sample and two aliquots were analysed, yielding slightly more complicated plateaus with an integrated age of ca. 122 Ma (Ootes et al., 2020b). The results indicate the granite cooled through the muscovite and biotite closure temperatures (ca. 350 to 300°C) between ca. 122 to 115 Ma. These cooling ages are interpreted to post-date the peak of regional deformation.

6.4. Mesilinka suite

Preliminary U-Pb zircon results from a K-feldspar phenocrystic granite sample (ca. 135 Ma; Schiarizza and Tan, 2005b) indicate many zircons are inherited from older crustal sources and the youngest zircons are ca. 135 Ma, providing a maximum crystallization age (Ootes et al., 2020b). Nine laser steps were conducted of biotite from a K-feldspar porphyritic granite sample (18lo12-7) and the results indicate an integrated $^{40}Ar/^{39}Ar$ age of 112.3 ±0.3 Ma, representing 76.81% of ^{39}Ar released (steps B-G; Fig. 10c; Table 2). The results indicate the granite cooled through the biotite closure temperature (ca. 300°C) at ca. 112 Ma. This age is interpreted to post-date regional deformation.

Biotite from a tonalite sample (ca. 174 Ma; Schiarizza and Tan, 2005b) was also analyzed and two separate aliquots yielded ca. 112 and 109 Ma ages. Mineral separates from a granodiorite phase yielded older ages, including biotite with a ca. 122.6 Ma $^{40}Ar/^{39}Ar$ cooling age and hornblende with a ca. 139 Ma $^{40}Ar/^{39}Ar$ cooling age. The ca. 140 Ma age may record the time of primary magmatic cooling.

7. Mineralization

Eighty-eight mineral occurrences in the area are documented in MINFILE (Fig. 11). Most can be considered as part of four end-member styles of mineralization. First, syngenetic porphyry-style Cu (±Au, Ag, Mo) mineralization is typically represented by malachite staining or disseminated chalcopyrite

Table 1. U-Th-Pb isotopic data.

	Compositional Parameters								Radiogenic Isotopes									Isotopic Ages					
Sample	Wt. mg	U ppm	Pb ppm	Th / U	$^{206}Pb^*$ x10^{-13} mol	mol % $^{206}Pb^*$ / Pb_c	Pb^* / Pb_c	Pb_c (pg)	^{206}Pb / ^{204}Pb	^{208}Pb / ^{206}Pb	^{207}Pb / ^{206}Pb	% err	^{207}Pb / ^{235}U	% err	^{206}Pb / ^{238}U	% err	corr. coef.	^{207}Pb / ^{206}Pb	±	^{207}Pb / ^{235}U	±	^{206}Pb / ^{238}U	±
(a)	(b)	(c)	(c)	(d)	(e)	(e)	(e)	(e)	(f)	(g)	(g)	(h)	(g)	(h)	(g)	(h)		(i)	(h)	(i)	(h)	(i)	(h)
18lo22-1a																							
A	0.0165	73	2.3	0.241	1.5655	99.12%	32	1.14	2111	0.077	0.05014	0.334	0.2150	0.390	0.03109	0.101	0.644	201.7	7.8	197.72	0.70	197.39	0.20
B	0.0125	67	2.1	0.262	1.0805	99.24%	37	0.68	2444	0.083	0.04999	0.307	0.2147	0.366	0.03115	0.111	0.642	194.3	7.1	197.46	0.66	197.73	0.22
C	0.0088	102	3.3	0.259	1.1718	98.53%	19	1.43	1261	0.083	0.05009	0.569	0.2149	0.628	0.03112	0.112	0.595	199	13	197.7	1.1	197.57	0.22
D	0.0099	157	4.9	0.243	2.0193	99.18%	34	1.37	2255	0.077	0.05008	0.334	0.2149	0.400	0.03112	0.135	0.616	198.7	7.8	197.64	0.72	197.56	0.26
18lo22-1d																							
A	0.0045	92	3.0	0.340	0.5343	98.14%	15	0.83	993	0.108	0.04996	0.733	0.2157	0.798	0.03131	0.114	0.620	193	17	198.3	1.4	198.74	0.22
B	0.0110	72	2.3	0.313	1.0364	99.02%	29	0.84	1897	0.099	0.05010	0.379	0.2152	0.434	0.03116	0.101	0.627	199.6	8.8	197.91	0.78	197.77	0.20
C	0.0107	123	3.9	0.346	1.7002	99.31%	42	0.97	2690	0.110	0.05007	0.284	0.2138	0.340	0.03097	0.097	0.673	198.2	6.6	196.73	0.61	196.61	0.19
D	0.0202	43	1.4	0.332	1.1321	99.02%	29	0.92	1893	0.106	0.05000	0.398	0.2153	0.455	0.03124	0.112	0.604	195.0	9.2	198.03	0.82	198.28	0.22
E	0.0291	30	1.0	0.421	1.1741	98.71%	23	1.26	1439	0.134	0.05032	0.508	0.2212	0.635	0.03188	0.323	0.609	210	12	202.9	1.2	202.28	0.64

(a) A, B etc. are labels for fractions composed of single zircon grains or fragments; all fractions annealed and chemically abraded after Mattinson (2005) and Scoates and Friedman (2008).
(b) Nominal fraction weights estimated from photomicrographic grain dimensions, adjusted for partial dissolution during chemical abrasion.
(c) Nominal U and total Pb concentrations subject to uncertainty in photomicrographic estimation of weight and partial dissolution during chemical abrasion.
(d) Model Th/U ratio calculated from radiogenic $^{208}Pb/^{206}Pb$ ratio and $^{206}Pb/^{238}U$ age.
(e) Pb* and Pbc represent radiogenic and common Pb, respectively; mol % $^{206}Pb^*$ with respect to radiogenic, blank and initial common Pb.
(f) Measured ratio corrected for spike and fractionation only. Mass discrimination of 0.25 ± 0.04%/amu based on analysis of NBS-982; all Daly analyses.
(g) Corrected for fractionation, spike, and common Pb; All common Pb was assumed to be procedural blank: $^{206}Pb/^{204}Pb$ = 18.50 ±1.0%; $^{207}Pb/^{204}Pb$ = 15.75 ±1.0%; $^{208}Pb/^{204}Pb$ = 38.40 ±1.0% (1σ errors).
(h) Errors are 2-sigma, propagated using the algorithms of Schmitz and Schoene (2007) and Crowley et al. (2007).
(i) Calculations are based on the decay constants of Jaffey et al. (1971). $^{206}Pb/^{238}U$ and $^{207}Pb/^{206}Pb$ ages corrected for initial disequilibrium in $^{230}Th/^{238}U$ using Th/U [magma] = 3.

Table 2a. Ar/Ar analytical data. Sample: 181o22-1d, biotite.

N		02A	02B	02C	02D	02E	02F	02G	02H	02I	**Age**
Power	%	0.2	1	1.3	1.6	1.9	2	2.3	3.5	6.5	
Age	(Ma)		119.7	122.9	124.4	124.7	124.9	124.7	123.1	124.5	**124.4**
±1σ	(Ma)		0.4	0.1	0.1	0.1	0.1	0.1	0.0	0.1	**0.7**
Ca/K			0.073	0.045	0.049	0.042	0.035	0.032	0.221	0.332	
±1σ			0.003	0.002	0.002	0.003	0.002	0.002	0.001	0.002	
Cl/K			0.000	0.000	0.000	0.000	0.000	0.000	0.000	0.000	
±1σ			0.001	0.000	0.000	0.001	0.001	0.000	0.000	0.000	
%^{40}Ar	(%)		47.79	77.21	91.10	95.58	95.56	95.46	94.96	94.85	
^{40}Ar*/^{39}Ar$_K$			3.639	3.739	3.786	3.795	3.801	3.794	3.744	3.788	
Corrected											
^{40}Ar	(fA)	0.34941	535.45794	583.88966	458.94563	289.97240	321.11499	441.30795	1008.52071	574.10785	
±1σ		0.03246	0.05814	0.06128	0.05701	0.04930	0.04787	0.04957	0.07328	0.06305	
^{39}Ar	(fA)	0.04913	70.26912	120.49689	110.37213	72.98369	80.67020	110.95525	255.62536	143.64570	
±1σ		0.01202	0.01726	0.02335	0.02268	0.01914	0.01842	0.02057	0.03411	0.02418	
^{38}Ar	(fA)	0.04955	1.02112	1.54145	1.33101	0.87092	0.96428	1.33507	3.10680	1.75978	
±1σ		0.01609	0.01637	0.01580	0.01485	0.01534	0.01704	0.01570	0.01602	0.01595	
^{37}Ar	(fA)	0.01008	0.35611	0.37455	0.37092	0.21077	0.19570	0.24391	3.86425	3.25987	
±1σ		0.01335	0.01359	0.01428	0.01390	0.01366	0.01375	0.01375	0.01396	0.01540	
^{36}Ar	(fA)	0.00042	0.94500	0.44815	0.13617	0.04194	0.04661	0.06550	0.17355	0.10313	
±1σ		0.00039	0.00263	0.00161	0.00100	0.00054	0.00063	0.00069	0.00109	0.00078	
Blanks											
^{40}Ar	(fA)	3.24651	2.77380	2.71458	3.88895	2.84610	3.26608	3.28220	2.81525	2.85239	
±1σ		0.02368	0.02392	0.02364	0.02288	0.02422	0.02121	0.02388	0.02112	0.02083	
^{39}Ar	(fA)	-0.00935	-0.00748	-0.00755	0.00598	0.02509	0.02232	0.02842	0.02756	0.05381	
±1σ		0.00885	0.00878	0.00887	0.00845	0.00904	0.00967	0.00836	0.00905	0.00922	
^{38}Ar	(fA)	-0.01959	0.01992	0.01535	0.02078	0.00748	0.00208	0.00520	0.00867	0.01629	
±1σ		0.01253	0.01134	0.01148	0.00996	0.01129	0.01130	0.01042	0.01012	0.01015	
^{37}Ar	(fA)	-0.01557	-0.02024	0.01072	0.00322	0.01013	0.02339	0.01371	0.00051	0.00699	
±1σ		0.00954	0.00952	0.00919	0.00931	0.01010	0.00975	0.00926	0.00947	0.01124	
^{36}Ar	(fA)	0.01083	0.00903	0.00926	0.01272	0.00885	0.01073	0.01030	0.00881	0.00822	
±1σ		0.00027	0.00022	0.00022	0.00026	0.00024	0.00028	0.00023	0.00023	0.00021	
IC^{CDD}		1.03104	1.03104	1.03104	1.03104	1.03104	1.03104	1.03104	1.03104	1.03104	
±1σ		0.00068	0.00068	0.00068	0.00068	0.00068	0.00068	0.00068	0.00068	0.00068	
Δt^3	(days)	112.55862	112.5891	112.61959	112.68424	112.71472	112.74524	112.81009	112.84072	112.87128	
J		0.0186	0.0186	0.0186	0.0186	0.0186	0.0186	0.0186	0.0186	0.0186	
±1σ		7.164E-05	7.164E-05	7.164E-05	7.164E-05	7.164E-05	7.164E-05	7.164E-05	7.164E-05	7.164E-05	
^{39}Ar Decay		1.000721	1.000721	1.000721	1.000721	1.000722	1.000722	1.000722	1.000723	1.000723	
^{37}Ar Decay		7.431369	7.435844	7.440325	7.449828	7.454315	7.458810	7.468369	7.472887	7.477401	
LambdaK		5.463E-10	5.463E-10	5.463E-10	5.463E-10	5.463E-10	5.463E-10	5.463E-10	5.463E-10	5.463E-10	
Irradiation		Can17E 6	Can17E 6	Can17E 6	Can17E 6	Can17E 6	Can17E 6	Can17E 6	Can17E 6	Can17E 6	

Table 2b. Ar/Ar analytical data. Sample: 181o17-1, biotite.

N		01A	01B	01C	01D	01E	01F	01G	01H	01I	**Age**
Power	%	0.2	1	1.3	1.6	1.9	2	2.3	3.5	6.5	
Age	(Ma)	133.6	105.9	116.1	116.7	116.9	116.3	115.6	114.8	112.9	**116.3**
±1σ	(Ma)	7.8	0.3	0.0	0.0	0.0	0.1	0.1	0.1	0.0	**0.5**
Ca/K		-0.028	0.016	0.006	0.009	0.012	0.024	0.022	0.047	0.193	
±1σ		0.322	0.001	0.000	0.001	0.001	0.002	0.001	0.001	0.000	
Cl/K		-0.003	0.000	0.000	0.000	0.000	-0.001	0.000	0.000	0.000	
±1σ		0.075	0.000	0.000	0.000	0.000	0.000	0.000	0.000	0.000	
%^{40}Ar	(%)	46.89	58.17	95.13	92.56	96.04	93.19	90.07	87.53	93.65	
^{40}Ar*/^{39}Ar$_K$		4.063	3.197	3.513	3.532	3.537	3.520	3.497	3.474	3.414	
Corrected											
^{40}Ar	(fA)	5.36295	1214.12544	1768.88282	1475.22441	850.40787	420.85736	487.08933	1123.30928	1684.08049	
±1σ		0.03467	0.07619	0.10459	0.09740	0.06660	0.05119	0.05548	0.08081	0.09826	
^{39}Ar	(fA)	0.61854	220.73267	478.65499	386.29563	230.74595	111.33094	125.38016	282.86170	461.61374	
±1σ		0.01318	0.02442	0.03636	0.03869	0.02868	0.01922	0.02267	0.03214	0.04008	
^{38}Ar	(fA)	0.00865	2.97674	5.78162	4.68674	2.74565	1.29959	1.53250	3.44122	5.59853	
±1σ		0.01592	0.01468	0.01598	0.01704	0.01588	0.01707	0.01619	0.01748	0.01543	
^{37}Ar	(fA)	-0.00127	0.26423	0.23014	0.27733	0.20579	0.20163	0.20782	0.97400	6.53509	
±1σ		0.01468	0.01447	0.01390	0.01427	0.01408	0.01400	0.01297	0.01319	0.01438	
^{36}Ar	(fA)	0.00962	1.71389	0.28033	0.36247	0.10853	0.09465	0.16094	0.46898	0.36280	
±1σ		0.00047	0.00585	0.00164	0.00174	0.00091	0.00086	0.00113	0.00211	0.00170	
Blanks											
^{40}Ar	(fA)	3.76014	3.50565	3.38754	4.06996	3.58692	3.57616	3.89730	3.85170	3.01199	
±1σ		0.02543	0.02276	0.02537	0.02123	0.02494	0.02217	0.02385	0.01965	0.02250	
^{39}Ar	(fA)	0.01603	0.00213	0.05272	0.04053	0.10374	0.06006	0.02596	0.05614	0.03263	
±1σ		0.00957	0.00863	0.00940	0.00948	0.00846	0.00885	0.00897	0.00892	0.00875	
^{38}Ar	(fA)	-0.01528	0.00089	0.00670	-0.00227	0.00561	0.02456	0.00888	-0.00034	-0.00849	
±1σ		0.01144	0.01045	0.01075	0.01082	0.01156	0.01215	0.01129	0.01170	0.01128	
^{37}Ar	(fA)	0.01475	0.01989	-0.00961	-0.01107	0.03367	-0.00072	0.00854	0.03253	0.03502	
±1σ		0.01033	0.01095	0.00980	0.01123	0.00936	0.01008	0.00867	0.00921	0.00921	
^{36}Ar	(fA)	0.01235	0.01140	0.01037	0.01268	0.01076	0.01147	0.01262	0.01229	0.00961	
±1σ		0.00024	0.00024	0.00024	0.00029	0.00025	0.00027	0.00025	0.00025	0.00023	
IC^{CDD}		1.03378	1.03378	1.03378	1.03378	1.03378	1.03378	1.03378	1.03378	1.03378	
±1σ		0.00305	0.00305	0.00305	0.00305	0.00305	0.00305	0.00305	0.00305	0.00305	
Δt^3	(days)	109.07263	109.10306	109.13353	109.19803	109.22852	109.25898	109.32353	109.35397	109.38443	
J		0.0186	0.0186	0.0186	0.0186	0.0186	0.0186	0.0186	0.0186	0.0186	
±1σ		5.216E-05	5.216E-05	5.216E-05	5.216E-05	5.216E-05	5.216E-05	5.216E-05	5.216E-05	5.216E-05	
^{39}Ar Decay		1.000696	1.000696	1.000696	1.000697	1.000697	1.000697	1.000698	1.000698	1.000698	
^{37}Ar Decay		6.936947	6.941117	6.945296	6.954149	6.958338	6.962526	6.971407	6.975600	6.979798	
LambdaK		5.463E-10	5.463E-10	5.463E-10	5.463E-10	5.463E-10	5.463E-10	5.463E-10	5.463E-10	5.463E-10	
Irradiation		Can17E 2	Can17E 2	Can17E 2	Can17E 2	Can17E 2	Can17E 2	Can17E 2	Can17E 2	Can17E 2	

Table 2c. Ar/Ar analytical data. Sample: 181o12-7, biotite.

N		01A	01B	01C	01D	01E	01F	01G	01H	01I	**Age**
Power	%	0.2	1	1.3	1.6	1.9	2	2.3	3.5	6.5	
Age	(Ma)		112.2	112.5	112.7	112.5	112.1	111.8	111.1	110.6	**112.3**
±1σ	(Ma)		0.1	0.0	0.0	0.1	0.1	0.1	0.1	0.1	**0.3**
Ca/K			0.002	0.003	0.007	0.017	0.040	0.021	0.039	0.703	
±1σ			0.006	0.002	0.002	0.003	0.004	0.004	0.002	0.004	
Cl/K			0.002	0.000	-0.001	0.000	-0.002	0.000	0.000	-0.002	
±1σ			0.001	0.000	0.000	0.001	0.001	0.001	0.001	0.001	
%^{40}Ar	(%)		97.01	97.93	97.88	96.78	96.51	97.23	95.88	95.33	
$^{40}Ar^*/^{39}Ar_K$			3.402	3.413	3.420	3.412	3.402	3.391	3.370	3.353	
Corrected											
^{40}Ar	(fA)	-0.33672	120.01286	398.27269	375.34799	245.83222	165.52959	162.98629	276.99555	167.74530	
±1σ		0.03137	0.03876	0.05064	0.05105	0.04034	0.03963	0.03843	0.04652	0.04075	
^{39}Ar	(fA)	0.09558	34.19651	114.19719	107.35892	69.67365	46.92505	46.69984	78.75325	47.67372	
±1σ		0.01395	0.01675	0.02294	0.02123	0.01840	0.01831	0.01734	0.01871	0.01698	
^{38}Ar	(fA)	0.00157	0.42943	1.36798	1.26223	0.82778	0.53388	0.56433	0.95132	0.53801	
±1σ		0.01609	0.01614	0.01530	0.01534	0.01607	0.01619	0.01514	0.01455	0.01601	
^{37}Ar	(fA)	0.00245	0.00476	0.02562	0.05481	0.08191	0.12883	0.06799	0.21242	2.26442	
±1σ		0.01479	0.01302	0.01527	0.01297	0.01343	0.01405	0.01395	0.01256	0.01288	
^{36}Ar	(fA)	-0.00266	0.01129	0.02515	0.02433	0.02521	0.01865	0.01426	0.03710	0.02993	
±1σ		0.00036	0.00041	0.00051	0.00048	0.00051	0.00046	0.00047	0.00060	0.00061	
Blanks											
^{40}Ar	(fA)	3.54869	2.89735	2.62744	3.56355	2.99392	2.75601	3.27554	2.72820	2.71520	
±1σ		0.02261	0.02043	0.02104	0.02377	0.02186	0.02136	0.02180	0.02419	0.02014	
^{39}Ar	(fA)	0.02535	0.00934	0.03037	0.03164	0.04759	0.03647	0.02026	0.02436	-0.00792	
±1σ		0.01019	0.00988	0.01050	0.00780	0.00908	0.00939	0.00861	0.00884	0.00841	
^{38}Ar	(fA)	0.00212	-0.00449	0.00389	0.00368	-0.00130	0.00654	-0.01138	-0.00245	0.01255	
±1σ		0.01065	0.01130	0.01140	0.01013	0.01099	0.01169	0.01071	0.01055	0.01102	
^{37}Ar	(fA)	0.01665	0.00211	0.00169	0.00366	-0.00788	-0.00684	0.00220	-0.00154	0.00714	
±1σ		0.01003	0.00953	0.01105	0.00858	0.01020	0.00994	0.01015	0.00918	0.00894	
^{36}Ar	(fA)	0.01180	0.00904	0.00826	0.01196	0.00949	0.00851	0.01078	0.00940	0.00862	
±1σ		0.00025	0.00023	0.00022	0.00027	0.00023	0.00021	0.00024	0.00024	0.00020	
IC^{CDD}		1.03107	1.03107	1.03107	1.03107	1.03107	1.03107	1.03107	1.03107	1.03107	
±1σ		0.00198	0.00198	0.00198	0.00198	0.00198	0.00198	0.00198	0.00198	0.00198	
Δt^3	(days)	113.10171	113.13229	113.16282	113.22774	113.25829	113.28885	113.35378	113.38444	113.41507	
J		0.0186	0.0186	0.0186	0.0186	0.0186	0.0186	0.0186	0.0186	0.0186	
±1σ		5.219E-05	5.219E-05	5.219E-05	5.219E-05	5.219E-05	5.219E-05	5.219E-05	5.219E-05	5.219E-05	
^{39}Ar Decay		1.000724	1.000725	1.000725	1.000725	1.000725	1.000726	1.000726	1.000726	1.000727	
^{37}Ar Decay		7.511508	7.516046	7.520580	7.530227	7.534772	7.539322	7.548997	7.553569	7.558139	
LambdaK		5.463E-10	5.463E-10	5.463E-10	5.463E-10	5.463E-10	5.463E-10	5.463E-10	5.463E-10	5.463E-10	
Irradiation		Can17E 7	Can17E 7	Can17E 7	Can17E 7	Can17E 7	Can17E 7	Can17E 7	Can17E 7	Can17E 7	

Integrated age (steps 2-7)
Notes:
1Corrected: Isotopic intensities corrected for blank, baseline, radioactivity decay and detector intercalibration, not for interfering reactions.
3Time interval (days) between end of irradiation and beginning of analysis.
fA = femto amps
Ages calculated relative to FC-1 Fish Canyon Tuff sanidine interlaboratory standard at 28.201+/-0 Ma

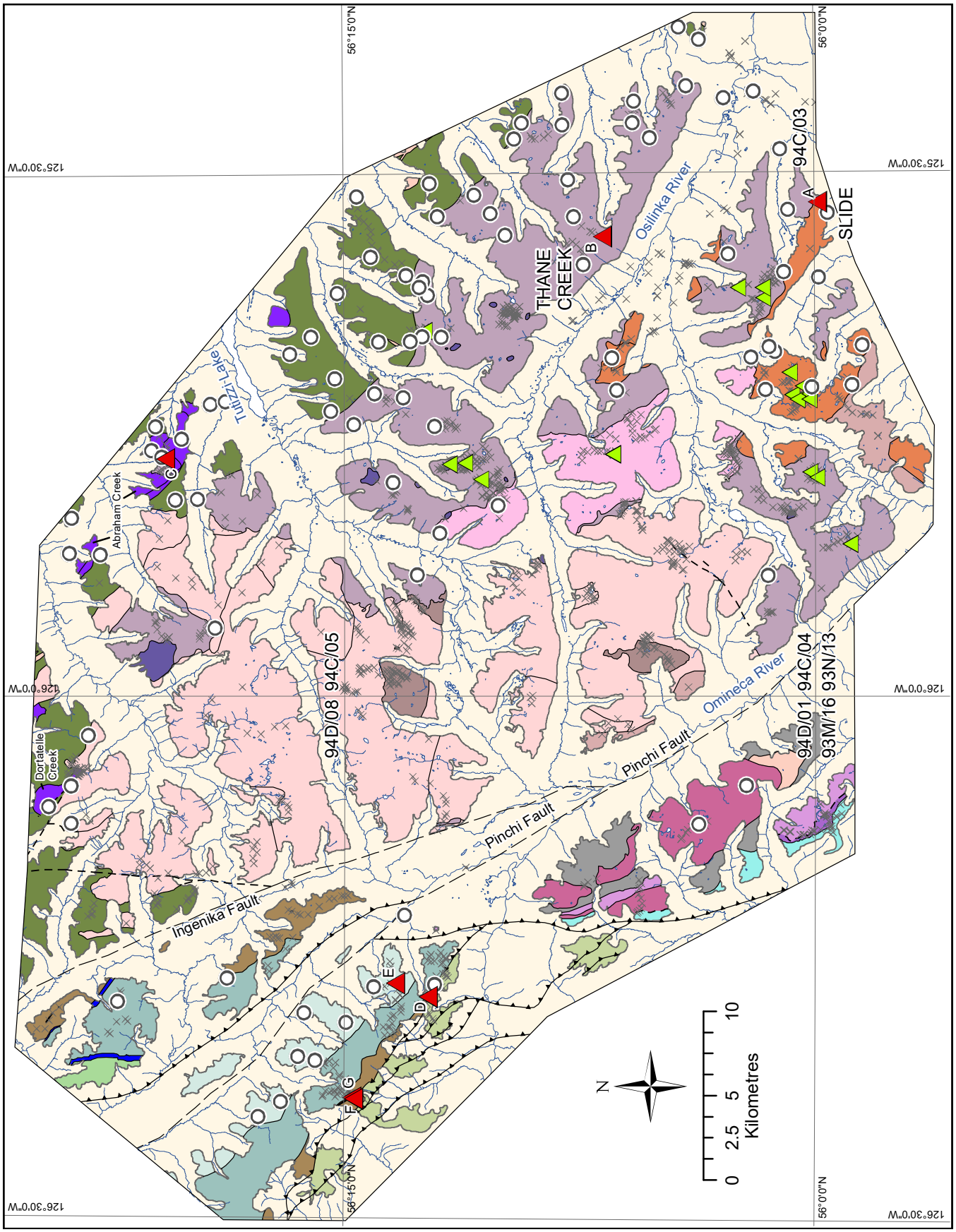

Fig. 11. Geology of northern Hogem batholith and surroundings with MINFILE and new mineral occurrences (see Table 3).

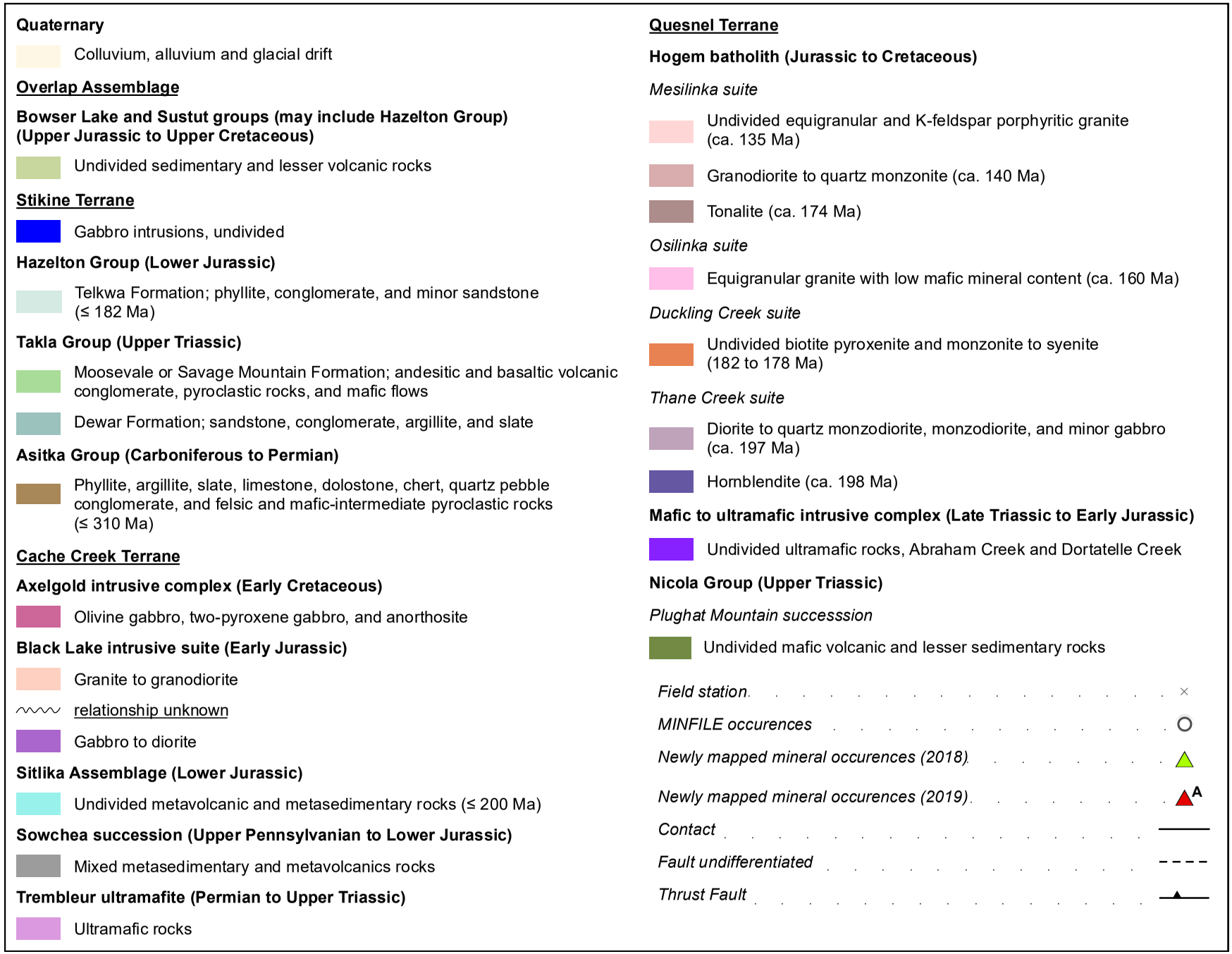

Fig. 11. Continued.

Table 3. Assay results from newly mapped mineral occurrences.

Label		**A**	**B**	**C**	**D**	**E**	**F**	**G**
station		GJO19-13-5b	GJO19-6-2	DMI19-24-3b	GJO19-19-5	GJO19-18-1	LOO19-4-2	LOO19-4-4
MINFILE		^Known SLIDE	^Known THANE CREEK	^Known WELT	^Known LEISHMAN	^Known ARP	New	New
Longitude		-125.526168	-125.558130	-125.769215	-126.285185	-126.272182	-126.381604	-126.383056
Latitude		55.999451	56.113880	56.34665	56.206991	56.224369	56.247218	56.246246
Au	ppb	110	3330	16	< 2	15	< 2	22
Ag	ppm	1.8	11.4	2.3	1.1	28.5	0.4	44.3
Cu	ppm	7010	8980	3120	9990	> 10000	1750	> 10000
Cd	ppm	< 0.3	0.6	1.1	< 0.3	3.5	0.4	4.2
Mo	ppm	44	2	111	< 1	3	< 1	2
Pb	ppm	6	3	13	13	6	4	11
Ni	ppm	7	3	101	9	25	18	2
Zn	ppm	55	13	50	62	70	67	105
S	%	0.43	0.76	0.85	0.65	0.4	0.05	1.52
Al	%	7.93	0.48	5.85	4.86	8.47	4.58	0.38
As	ppm	2.2	3.1	< 0.5	3.8	7.4	2.8	12.1
Ba	ppm	2010	< 50	680	< 50	490	170	< 50
Be	ppm	1	< 1	< 1	< 1	< 1	< 1	< 1
Bi	ppm	5	< 2	< 2	< 2	3	< 2	< 2
Br	ppm	< 0.5	< 0.5	< 0.5	< 0.5	< 0.5	< 0.5	< 0.5
Ca	%	1.13	5.11	0.97	12.9	4.3	6.41	0.7
Co	ppm	11	3	60	14	25	25	4
Cr	ppm	12	31	331	34	62	55	34
Cs	ppm	< 1	< 1	1	< 1	< 1	< 1	< 1
Eu	ppm	0.2	0.2	< 0.2	0.6	0.5	0.8	< 0.2
Fe	%	3.27	2.36	24.4	4.19	4.49	5.78	2.57
Hf	ppm	3	< 1	< 1	1	2	3	< 1
Hg	ppm	< 1	< 1	< 1	< 1	< 1	< 1	< 1
Ir	ppb	< 5	< 5	< 5	< 5	< 5	< 5	< 5
K	%	4.96	0.07	1.27	0.06	1.21	0.28	0.05
Li	ppm	13	4	12	12	9	14	2
Mg	%	0.57	0.18	0.84	1.29	1.7	1.39	0.05
Mn	ppm	376	1170	503	1140	1140	1880	355
Na	%	2.24	0.05	3.23	2.72	1.99	2	0.11
P	%	0.078	0.005	0.002	0.07	0.105	0.088	0.012
Rb	ppm	127	< 15	< 15	< 15	< 15	< 15	< 15
Sb	ppm	0.3	1.3	0.2	0.4	0.8	< 0.1	3.7
Sc	ppm	4.3	1.1	4.8	10.4	18.8	19	1.1
Se	ppm	< 3	< 3	< 3	< 3	41	< 3	< 3
Sr	ppm	376	137	216	208	553	243	23
Ta	ppm	< 0.5	< 0.5	< 0.5	< 0.5	< 0.5	< 0.5	< 0.5
Ti	%	0.22	< 0.01	0.1	0.25	0.38	0.26	0.03
Th	ppm	4.9	< 0.2	< 0.2	1	2	0.8	0.2
U	ppm	1.9	< 0.5	< 0.5	< 0.5	< 0.5	1.4	< 0.5
V	ppm	79	9	607	135	209	84	9
W	ppm	7	< 1	< 1	< 1	< 1	< 1	< 1
Y	ppm	10	6	< 1	12	19	19	2
La	ppm	13.5	2.5	0.8	6.1	8.6	7.7	0.7
Ce	ppm	22	5	< 3	16	21	21	< 3
Nd	ppm	10	< 5	< 5	7	14	9	< 5
Sm	ppm	1.7	0.8	0.1	1.8	2.8	2.8	0.2
Sn	%	0.03	< 0.02	< 0.02	< 0.02	< 0.02	< 0.02	< 0.02
Tb	ppm	< 0.5	< 0.5	< 0.5	< 0.5	< 0.5	< 0.5	< 0.5
Yb	ppm	1.1	0.4	< 0.2	1	1.8	1.9	< 0.2
Lu	ppm	0.08	< 0.05	< 0.05	< 0.05	0.11	0.06	< 0.05
Mass	g	31.7	33.8	38.0	37.0	36.3	32.7	35.2

Labels correspond to locations plotted on Figure 11; underlined values are considered of interest; ^close to mineralization documented in MINFILE

in the host-rock. The mineral showings of this type are hosted in the Thane Creek and Duckling Creek suites, or in Nicola Group adjacent to Hogem batholith. One porphyry Mo-showing is related to the Mesilinka granite and one to the Osilinka granite. The second style of mineralization is related to mafic and ultramafic intrusive rocks and includes Ni-Cu ±PGE in the Axelgold layered mafic intrusion, Alaskan-type chromite near the Dortatelle Creek mafic-ultramafic intrusion, and podiform chromite in a Cache Creek serpentinite. The third type is volcanic- and sediment-hosted Cu, which is typically stratabound in the Telkwa Formation of the Hazelton Group. The fourth style includes epigenetic quartz veins with local concentrations of precious and base metals (e.g., Hawk showing; Nelson et al., 2001). Other types of mineralization in the area are also reported in MINFILE (e.g., Besshi-type massive sulphides.

During mapping, we collected representative grab samples with metallic mineralization from outcrops. These samples were sent to Activation Laboratories (Ancaster, Ontario) where they were analyzed by a combination of instrumental neutron activation analysis (INAA) and acid dilution inductively coupled plasma-mass spectrometry (ICP-MS Table 3; Ootes et al., 2020b). To the 17 mineral occurrences discovered in 2018 (Ootes et al., 2019), we add seven new ones, five of which are close to previously documented mineralization (Fig. 11; Table 3).

All the documented occurrences are Cu-bearing, and one (B) contains ~3 ppm Au. On Figure 11, result A is close to the Slide showing in the Duckling Creek syenite and B is near the Thane Creek showing in the Thane Creek diorite, both of which are interpreted as alkalic porphyry Cu-type mineralization. Result C is adjacent to the Welt polymetallic vein showing, D is volcanic-hosted Cu, close to the Leishmann volcanic redbed Cu showing in undivided Bowser Lake and Sustut groups, and E is sediment-hosted Cu, close to the Arp volcanic redbed Cu showing in the Telkwa Formation. Results F and G are new Cu occurrences that are hosted in quartz veins that cut the Asitka Group.

8. Summary

This study provides a preliminary overview of the geology of the northern Hogem batholith and its surrounding rocks in the Quesnel, Stikine, and Cache Creek terranes. The first modern U-Pb zircon and Ar-Ar laser step heating results indicate the earliest intrusive phases in Hogem batholith are ca. 197 Ma hornblendite and diorite of the Thane Creek suite (Fig. 4). The Duckling Creek syenite was emplaced between 182 and 178 Ma, the Osilinka suite granite at ca. 160 Ma, or younger, and the Mesilinka suite tonalite at ca. 174 Ma, and granodiorite and granites at ca. 140 Ma. Foliation-defining biotite preserves 125 to 110 Ma ages, indicating post-deformation cooling and uplift. The results indicate that a regional contractional deformation event affected the Hogem batholith between 140 and 125 Ma.

The Thane Creek suite rocks in Hogem batholith have undergone at least two stages of deformation and the youngest, the rocks of the Mesilinka suite, are deformed (Ootes et al., 2019). Multigenerational fabrics are also developed in rocks of the Stikine and Cache Creek terranes; further evaluation of the structural relationship between these three terranes is ongoing.

Assay samples collected during bedrock mapping identify new mineralized horizons, five of which are close to documented occurrences and two occur as quartz vein-hosted Cu in the Asitka Group (Table 3). When combined with the results of 2018 mapping, the project has identified 24 mineral occurrences in addition to 88 previously documented. This supports that the study area is prospective for mineral resources.

Acknowledgments

Field assistance in 2019 was from Dylan Spence, Jade Lockie, Kristian Shortridge, and Moe Farhat, and 2018 field assistance was from Ben Graham, Dylan Spence, Silken Rauhala, and Reid Simmonds. We thank Silver King helicopters for air support, Cassiar Geoscience for expediting services, and the Abraham family for accommodations. Ongoing interest and support from the Tsay Keh Dene First Nation is appreciated. A field visit with Don Bragg and Jarrod Put helped improve our understanding of some parts of the southeastern Hogem batholith. Discussions with colleagues at the BC Geological Survey improved our understanding of the regional geology. Reviews by F. Ferri and L. Aspler helped improve the clarity of the manuscript.

References cited

Armstrong, J.E., 1946. Aiken Lake (south half), British Columbia. Geological Survey of Canada, Paper 46-11, 1 sheet, scale 1 inch:2 miles.

Armstrong, J.E., 1948. Fort St. James, British Columbia. Geological Survey of Canada, A Series Map 907A, scale 1inch:4 miles.

Armstrong, J.E., and Roots, E.F., 1948. Aiken Lake map-area, British Columbia. Geological Survey of Canada, Paper 48-5, 46 p.

Armstrong, J.E., and Roots, E.F., 1954. Aiken Lake, Cassiar District, British Columbia. Geological Survey of Canada, A Series Map 1030A, scale 1inch:4 miles.

Armstrong, R.L., Monger, J.W.H., and Irving, E., 1985. Age of magnetization of the Axelgold Gabbro, north-central British Columbia. Canadian Journal of Earth Sciences, 22, 1217-1222.

Bath, A.B., Cooke, D.R., Friedman, R.M., Faure, K., Kamenetsky, V.S., Tosdal, R.M., and Berry, R.F., 2014. Mineralization, U-Pb geochronology, stable isotope geochemistry of the Lower Main Zone of the Lorraine deposit, north-central British Columbia: A replacement-style alkalic Cu-Au porphyry. Economic Geology, 109, 979-1004.

CGG Canada Services Ltd., 2018. Geophysical survey report MIDAS high resolution magnetic and radiometric survey Search Project Phase III. Geoscience BC Report 2018-2.

Devine, F.A.M., Chamberlain, C.M., Davies, A.G.S., Friedman, R., and Baxter, P., 2014. Geology and district-scale setting of tilted alkalic porphyry Cu-Au mineralization at the Lorraine deposit, British Columbia. Economic Geology, 109, 939-977.

Evenchick, C.A., Mustard, P.S., McMechan, M., Ferri, F., Porter, S., Hadlari, T., and Jakobs, G., 2007. Geology, McConnell Creek, British Columbia. Geological Survey of Canada, Open File 5571, British Columbia Ministry of Energy, Mines and Petroleum Resources, Petroleum Geology Open File 2007-10, scale 1:125,000.

Evenchick, C.A., McMechan, M., Mustard, P.S., Ritcey, D.H., Smith, G.T., Ferri, F., and Waldron, JW.F., 2008. Geology, Hazelton, British Columbia. Geological Survey of Canada, Open File 5704, British Columbia Ministry of Energy, Mines and Petroleum Resources, Petroleum Geology Open File 2008-06, scale 1:125,000.

Ferri, F., Dudka, S, Rees, C., and Meldrum, D., 1993. Geology of the Aiken Lake area and Osilinka River areas, northern Quesnel Trough (NTS 94C/2, 3, 5, 6 & 12). British Columbia Ministry of Energy, Mines and Petroleum Resources, British Columbia Geological Survey Paper 1993-1, pp. 109-134.

Ferri, F., Dudka, S.F., Rees, C., and Meldrum, D., 2001a. Geology of the Aiken Lake area, north-central British Columbia, NTS 94C/5, 6 and 12. British Columbia Ministry of Energy, Mines and Petroleum Resources, British Columbia Geological Survey Geoscience Map 2001-10, scale 1:50,000.

Ferri, F., Dudka, S.F., Rees, C.J., Meldrum, D.G., and Willson, M.J., 2001b. Geology of the Uslika Lake Area, North-Central B.C. (NTS 94C/2, 3 & 4). British Columbia Ministry of Energy, Mines and Petroleum Resources, British Columbia Geological Survey Geoscience Map 2001-04, scale 1:50,000.

Garnett, J.A., 1972, Preliminary geological map of part of Hogem batholith, Duckling Creek area (parts of NTS 93N/13, 14; 94C/3, 4). British Columbia Ministry of Energy, Mines and Petroleum Resources, British Columbia Geological Survey Preliminary Map 09.

Garnett, J.A., 1978. Geology and mineral occurrences of the southern Hogem batholith. British Columbia Ministry of Energy, Mines and Petroleum Resources, British Columbia Geological Survey Bulletin 70, 75 p.

Irvine, T.N., 1975. Axelgold layered gabbro intrusion, McConnell Creekmap-area, British Columbia. Geological Survey of Canada Paper 75-1B, pp. 81-88.

Irvine, T.N., 1976. Studies of Cordilleran gabbroic and ultramafic intrusions, British Columbia. Geological Survey of Canada, Paper 76-1A, 75-81.

Irving, E., and Monger, J.W.H., 1987. Preliminary paleomagnetic results from the Permian Asitka Group, British Columbia. Canadian Journal of Earth Sciences, 24, 1490-1497.

Jaffey, A.H., Flynn, K.F., Glendenin, L.E., Bentley, W.C., and Essling, A.M., 1971. Precision measurement of half-lives and specific activities of ^{235}U and ^{238}U. Physical Review C, 4, 1889-1906.

Logan, J.M., Schiarizza, P., Struik, L.C., Barnett, C., Nelson, J.L., Kowalczyk, P., Ferri, F., Mihalynuk, M.G., Thomas, M.D., Gammon, P., Lett, R., Jackaman, W., and Ferbey, T., 2010. Bedrock Geology of the QUEST map area, central British Columbia. British Columbia Geological Survey Geoscience Map 2010-1, Geoscience BC Report 2010-5, Geological Survey of Canada Open File 6476, scale 1:500,000.

Lord, C.S., 1948. McConnell Creek map-area, Cassiar District, British Columbia. Geological Survey of Canada, Memoir 251, 82 p.

Lord, C.S., 1949. McConnell Creek, Cassiar District, British Columbia. Geological Survey of Canada, A Series Map 962A, scale 1inch:4 miles.

Massey, N.W.D., MacIntyre, D.J., Desjardins, P.J., and Cooney, R.T., 2005a. Digital geology map of British Columbia: whole province. British Columbia Ministry of Energy, Mines and Petroleum Resources, British Columbia Geological Survey GeoFile 2005-1, scale 1:250,000.

Massey, N.W.D., MacIntyre, D.G., Okulitch, A.V., Desjardins, P.J., and Cooney, R.T., 2005b. Digital geology map of British Columbia: Tile No10 northeast B.C., British Columbia Ministry of Energy, Mines and Petroleum Resources, British Columbia Geological Survey GeoFile 2005-10, scale 1:250,000.

Min K., Mundil R., Renne P.R. and Ludwig K.R., 2000. A test for systematic errors in $^{40}Ar/^{39}Ar$ geochronology through comparison with U-Pb analysis of a 1.1 Ga rhyolite. Geochimica et Cosmochimica Acta, 64, 73-98.

Monger, J.W.H., 1974. Upper Paleozoic and Lower Mesozoic rocks of the Omineca Mountains. Geological Survey of Canada, Paper 74-1A, pp. 19-20.

Monger, J.W.H., 1977. The Triassic Takla Group in McConnell Creek map-area, north-central British Columbia. Geological Survey of Canada, Paper 76-29, 45 p.

Mortensen, J.K., Ghosh, D.K., and Ferri, F., 1995. U-Pb geochronology of intrusive rocks associated with copper-gold porphyry deposits in the Canadian Cordillera. Canadian Institute of Mining, Metallurgy and Petroleum, Special Volume 46, pp. 142-158.

Nelson, J., Carmichael, B., and Gray, M., 2003. Innovative gold targets in the Pinchi Fault/Hogem Batholith area: The Hawk and Axelgold properties, central British Columbia (94C/4, 94N/13). British Columbia Ministry of Energy, Mines and Petroleum Resources, British Columbia Geological Survey Paper 2003-1, pp. 97-114.

Nelson, J.L., Colpron, M., and Israel, S., 2013. The Cordillera of British Columbia, Yukon, and Alaska: Tectonics and metallogeny. In: Colpron, M., Bissing, T., Rusk, B.G., and Thompson, J.F.H., (Eds.), Tectonics, Metallogeny, and Discovery: The North American Cordillera and similar accretionary settings. Society of Economic Geologists, Special Publication 17, pp. 53-109.

Nixon, G.T., and Peatfield, G.R., 2003. Geological setting of the Lorraine Cu-Au porphyry deposit, Duckling Creek syenite complex, north-central British Columbia. British Columbia Ministry of Energy, Mines and Petroleum Resources, British Columbia Geological Survey Open File 2003-4, 24 p.

Ootes, L., Bergen, A.L., Milidragovic, D., and Graham, B., 2019a. Bedrock geology of Notch Peak and Ogden Creek (parts of NTS 094C/04 and 093N/13), northern Hogem batholith, Quesnel terrane, north-central British Columbia. British Columbia Ministry of Energy, Mines and Petroleum Resources, British Columbia Geological Survey Open File 2019-02, scale 1:50,000.

Ootes, L., Bergen, A., Milidragovic, D., Graham, B., and Simmonds, R., 2019b. Preliminary geology of northern Hogem batholith, Quesnel terrane, north-central British Columbia. British Columbia Ministry of Energy, Mines and Petroleum Resources, British Columbia Geological Survey Paper 2019-01, pp. 31-53.

Ootes, L., Bergen, A.L., Milidragovic, D., and Jones, G.O., 2020a. Preliminary geology of the northern Hogem batholith and its surroundings, north-central British Columbia. British Columbia Ministry of Energy, Mines and Petroleum Resources, British Columbia Geological Survey Open File 2020-02, scale 1:50,000.

Ootes, L., Milidragovic, D., Camacho, A., Jones, G.O., Luo, Y., Pearson, G.D., and Friedman, R., 2020b. Geochronologic and geochemical data from northern Hogem batholith and its surroundings, north-central British Columbia. British Columbia Ministry of Energy, Mines and Petroleum Resources, British Columbia Geological Survey GeoFile, in prep.

Paterson, I.A., 1974. Geology of the Cache Creek Group and Mesozoic rocks at the northern end of the Stuart Lake belt, central British Columbia. Geological Survey of Canada, Paper 74-1B, 31-42.

Roots, E.F., 1954. Geology and mineral deposits of Aiken Lake map-area, British Columbia. Geological Survey of Canada, Memoir 274, 246 p.

Schiarizza, P., 2000. Old Hogem (western part), NTS 93N/11, 12, 13. British Columbia Ministry of Energy and Mines, British Columbia Geological Survey Open File 2000-33, scale 1:100,000.

Schiarizza, P., 2016. Toward a regional stratigraphic framework for the Nicola Group: Preliminary results from the Bridge Lake-

Quesnel River area. British Columbia Ministry of Energy and Mines, British Columbia Geological Survey Paper 2016-1, pp. 13-30.

Schiarizza, P., 2019. Geology of the Nicola Group in the Bridge Lake-Quesnel River area, south-central British Columbia. British Columbia Ministry of Energy, Mines and Petroleum Resources, British Columbia Geological Survey Paper 2019-01, pp. 15-30.

Schiarizza, P., and Tan, S.H., 2005a. Geology and mineral occurrences of the Quesnel Terrane between the Mesilinka River and Wrede Creek (NTS 94D/8, 9), north-central British Columbia. British Columbia Ministry of Energy and Mines, British Columbia Geological Survey Paper 2005-1, pp. 109-130.

Schiarizza, P., and Tan, S.H., 2005b. Geology of the Johanson Lake area, parts of NTS 94D/8 and 9. British Columbia Ministry of Energy, Mines and Petroleum Resources, British Columbia Geological Survey Open File 2005-4, scale 1:50,000.

Steiger R.H., and Jäger E., 1977. Subcommission on geochronology: convention on the use of decay constants in geo- and cosmochronology. Earth and Planetary Science Letters, 36, 359-362.

Tipper, H.W., and Richards, T.A., 1976. Jurassic stratigraphy and history of north-central British Columbia. Geological Survey of Canada, Bulletin 270, 73 p.

Woodsworth, G.J., 1976. Plutonic rocks of McConnell Creek (94 D west half) and Aiken Lake (94 C east half) map-areas, British Columbia. Geological Survey of Canada, Paper 76-1A, 69-73.

Woodsworth, G.J., Anderson, R.G., and Armstrong, R.L., 1991. Plutonic regimes, Chapter 15, In: Gabrielse, H., and Yorath, C.J., (Eds.), Geology of the Cordilleran Orogen in Canada, Geological Survey of Canada, Geology of Canada, no. 4, 491-531.